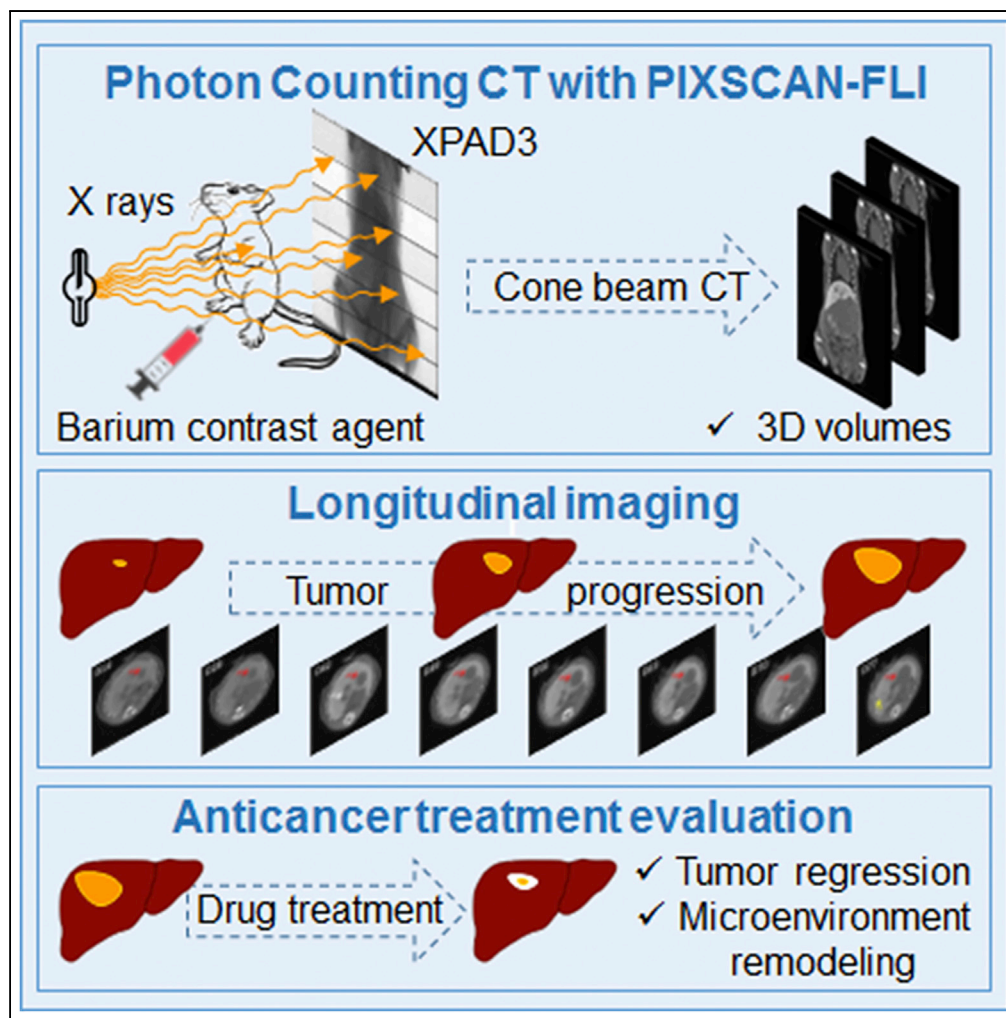**Article**

Tracking Dynamics of Spontaneous Tumors in Mice Using Photon-Counting Computed Tomography

Franca Cassol, Loriane Portal, Sylvie Richelme, ..., Toby Lawrence, Christian Morel, Flavio Maina

morel@cppm.in2p3.fr (C.M.)
flavio.maina@univ-amu.fr (F.M.)

HIGHLIGHTS

Development of photon-counting micro-computed tomography (PC-CT) with hybrid pixels

PC-CT allows longitudinal imaging of tumor dynamics in mouse cancer models

RTK-driven tumors are heterogeneous at onset, but grow steadily during progression

MEK + BCL-XL targeting leads to tumor regression and microenvironment remodeling

Article

Tracking Dynamics of Spontaneous Tumors in Mice Using Photon-Counting Computed Tomography

Franca Cassol,[1,5] Loriane Portal,[1,5] Sylvie Richelme,[2] Mathieu Dupont,[1] Yannick Boursier,[1] Maria Arechederra,[2] Nathalie Auphan-Anezin,[3] Lionel Chasson,[3] Caroline Laprie,[3] Samantha Fernandez,[4] Laure Balasse,[4] Fabienne Lamballe,[2] Rosanna Dono,[2] Benjamin Guillet,[4] Toby Lawrence,[3] Christian Morel,[1,6,*] and Flavio Maina[2,6,7,**]

SUMMARY

Computed tomography is a powerful medical imaging modality for longitudinal studies in cancer to follow neoplasia progression and evaluate anticancer therapies. Here, we report the generation of a photon-counting micro-computed tomography (PC-CT) method based on hybrid pixel detectors with enhanced sensitivity and precision of tumor imaging. We then applied PC-CT for longitudinal imaging in a clinically relevant liver cancer model, the _Alb-R26^{Met}_ mice, and found a remarkable heterogeneity in the dynamics for tumors at the initiation phases. Instead, the growth curve of evolving tumors exhibited a comparable exponential growth, with a constant doubling time. Furthermore, longitudinal PC-CT imaging in mice treated with a combination of MEK and BCL-XL inhibitors revealed a drastic tumor regression accompanied by a striking remodeling of macrophages in the tumor microenvironment. Thus, PC-CT is a powerful system to detect cancer initiation and progression, and to monitor its evolution during treatment.

INTRODUCTION

In vivo non-invasive longitudinal monitoring in cancer mouse models is a powerful strategy to follow over time the progression of tumors in the same animal (Anton et al., 2017). Among available methods, X-ray micro-computed tomography (CT) has gained significant interest for a series of advantages it offers (Ashton et al., 2015; Martiniova et al., 2010; Schambach et al., 2010; Wathen et al., 2013). Besides the relatively fast and easy process required, the high spatial resolution achieved (~10–100 μm) provides detailed anatomical information of tumors in the host organ. Micro-CT allows generating tomographic data that can be subsequently processed for a 3D reconstruction of the tumor area. The availability of several formulations of contrast agents has further implemented the micro-CT imaging approach in cancer animal models, permitting visualization of tumors and metastasis in different organs (Boll et al., 2011; Mannheim et al., 2016). In particular, a set of contrast agents has been developed for micro-CT imaging of tumors in the liver for mouse preclinical studies (Anton et al., 2017; Boll et al., 2011; Rothe et al., 2015; Willekens et al., 2009). Among these contrast agents, the commercially available ExiTron nano 12000 (Miltenyi Biotec GmbH, Germany), which can be injected in small volumes, exhibits high amount of X-ray absorption being an alkaline earth metal nanoparticle, thus offering excellent attenuation and contrast enhancement (Boll et al., 2013; Liu et al., 2019; Wathen et al., 2013). ExiTron nano 12000 is phagocytized and accumulated by macrophages in the spleen and Kupffer cells in the reticuloendothelial system of the liver. Kupffer cells are resident liver macrophages essential for tissue physiology and homeostasis (Krenkel and Tacke, 2017), ensuring as well host defense through phagocytosis of particles such as the contrast ExiTron nano 12000 that we used in our studies. Consequently, both spleen and liver are highly contrasted by micro-CT imaging. Anatomical evaluations of the spleen and the liver in normal and regenerative processes using ExiTron nano 12000 have been reported (Das et al., 2016; Will et al., 2017). Importantly, ExiTron nano 12000 does not cause hepatotoxicity and does not lead to pro-inflammatory cytokine release in the liver or serum, thus ensuring a relatively safe approach for longitudinal pharmacology and toxicology studies (Boll et al., 2011, 2013; Liu et al., 2019; Mannheim et al., 2016). This approach turned out to be very powerful for imaging primary tumors or metastases in the liver, which appear in negative because they lack contrast agents, as opposed to the liver, which is highly contrasted because of the high proportion of macrophages in the reticuloendothelial system (Bour et al., 2014; Pandit et al., 2013). However, several limitations should still

be overcome, including the quality required for quantitative image processing, radiation doses, and small tumor detectability.

In the present study, we report the development of a micro-CT scanner prototype named PIXSCAN-FLI based on hybrid pixel detectors (Ballabriga et al., 2016; Cassol et al., 2009; Delpierre, 2014; Wermes, 2005) to perform photon-counting (PC)-CT scans of mice (Cassol et al., 2016; Taguchi and Iwanczyk, 2013). PC-CT allows reducing the required dose of radiation received by the mice, thus limiting the damaging effects after multiple scans that might affect tissue homeostasis and the mouse life. We then applied this system for longitudinal studies in a clinically relevant liver tumor mouse model, the $Alb-R26^{Met}$ mice. We have previously reported that $Alb-R26^{Met}$ mice, carrying a slight upregulation of the receptor tyrosine kinase (RTK) MET in the liver, spontaneously develop liver tumors overtime, further progressing into hepatocellular carcinoma (HCC) (Fan et al., 2015, 2017, 2019; Genestine et al., 2011; Tonges et al., 2011). Importantly, the $Alb-R26^{Met}$ HCC model recapitulates the "proliferative-progenitor" HCC patient subgroup (Arechederra et al., 2018; Fan et al., 2017). Therefore the $Alb-R26^{Met}$ liver cancer model offers the unique possibility to follow initiation, latency, and evolution of spontaneous tumors, in contrast to other preclinical systems based on single-tumor formation following experimental implantation of HCC cells in the liver of nude or syngeneic mice. We show that the PIXSCAN-FLI prototype can be used efficiently to perform qualitative analyses and quantitative measurements of spontaneous liver tumors. Furthermore, high contrast and spatial resolution was achieved with radiation doses that did not induce noticeable side effects, thus allowing longitudinal studies with multiple scans up to 3 months. We high-lighted the temporal dynamics of tumor growth in normal condition, during and after combinatorial drug treatments. Combined imaging and marker analysis provided insights into a remodeling process involving macrophages in the tumor microenvironment occurring during drug-triggered tumor regression.

RESULTS

The PIXSCAN-FLI PC-CT Prototype Permitted Long-Term Longitudinal Imaging with High Contrast and Spatial Resolution of Spontaneous Liver Tumors

We developed a micro-CT scanner prototype for non-invasive imaging of small animals named PIXSCAN-FLI (Figure S1). This scanner was equipped with a hybrid pixel XPAD3 camera (Cassol et al., 2009; Pangaud et al., 2007). Hybrid pixels consist of a pixelated sensor wherein each pixel is physically bound to its readout electronics integrated in a chip. Their principal innovative characteristic relies on the digital conversion of the X-ray photons that give a signal higher than a predefined threshold. Hence, hybrid pixels provide PC instead of integrating the overall signal charge generated by the X-ray beam. This feature allowed a linear detector response free from electronic noise (Cassol et al., 2009), thus minimizing the X-ray flux and the dose delivered to the animal (Cassol et al., 2016). We optimized the scanner acquisition parameters (50 kV/500 μA, 0.6 mm Al filtering, 720 projections) to reach a low radiation dose (180 mGy/scan), thus preventing radiobiological effects along repeated scans and maximizing contrast-to-noise ratio observed for a contrast phantom QRM-microCT-HA (QRM GmbH, Germany). Notably, the PIXSCAN-FLI prototype allows performing a full-body scan of adult mice, in contrast with other micro PC-CT scanners. For *in vivo* imaging, mice were placed in vertical position on the PC-CT rotation table (Figure S1) and remained under isoflurane anesthesia during the whole scan, which lasted for 7.5 min.

The PIXSCAN-FLI prototype was used for longitudinal PC-CT imaging of liver tumors. For this purpose, the $Alb-R26^{Met}$ liver cancer genetic model was particularly appropriate, as spontaneous tumor formation and progression to HCC occurs in these mice, with a frequency ranging from 42% to 79% at the age of 40–48 weeks and >67 weeks, respectively (Fan et al., 2017). Consequently, the $Alb-R26^{Met}$ model allows detecting endogenous tumors at initiation stages and following their progression overtime, in contrast to other models previously used for longitudinal micro-CT imaging based on the HCC cell implantation into the liver. Small tumor detectability is affected by the noise of the system (Cassol et al., 2016; Hanson, 1979), which in the case of PC is only related to the counting statistics, and hence to the delivered dose. Moreover, it depends on the intrinsic contrast of the lesion and on its dimension. Therefore, to improve the detectability of small tumors, we used a contrast agent, which increased the intrinsic contrast between the tumors and the healthy liver tissue. To maximize visualization and detection of soft tissues in parenchymal organs, we selected the ExiTron nano 12000, a long-lasting contrast agent based on barium nanoparticles. This approach ensures great parenchymal contrast in the liver and spleen as the high metal load particles are taken up by macrophages. ExiTron nano 12000 increased by a factor of 5 the liver tissue X-ray attenuation coefficient, with a maximum tissue contrast 24 h after a 4 μL/g mouse of injected agent
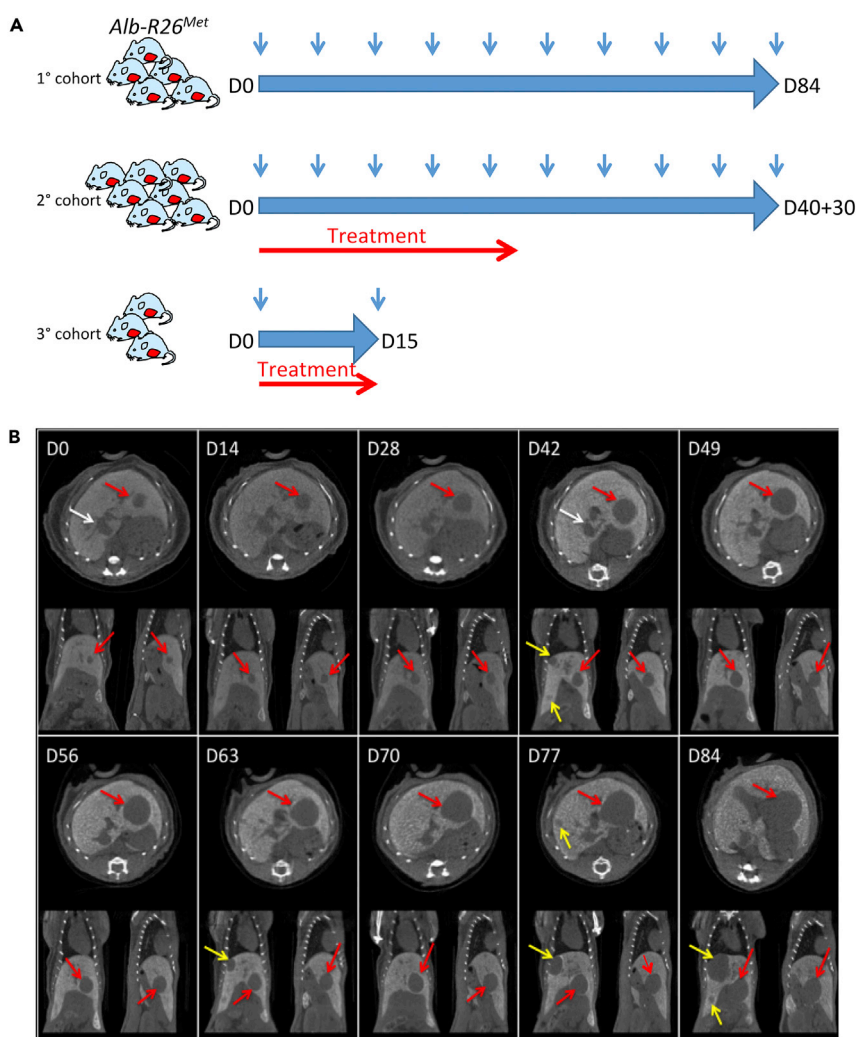
Figure 1. Longitudinal *In Vivo* PC-CT Imaging of Spontaneous Liver Tumor Dynamics in the *Alb-R26^Met* Model

(A) Schematic representation of longitudinal *in vivo* imaging studies that we performed to follow tumor initiation and evolution over time in the *Alb-R26^Met* mouse model. Three cohorts were used for imaging of untreated mice (1° cohort), mice treated with drug combinations (2° cohort), and mice with a short treatment with drug combinations to perform histological studies (3° cohort).

(B) Example of longitudinal monitoring of liver tumor growth in an *Alb-R26^Met* mouse (M1) with the PIXSCAN-FLI PC-CT prototype. For this representative mouse, image monitoring was performed at D0, D14, D28, D42, D49, D56, D63, D70, D77, and D84. For each day of monitoring, transversal (top), coronal (left bottom), and sagittal (right bottom) slices are shown. The red arrows indicate tumor already detected at D0. The white arrows at D0 and D42 point to the venae cava. The yellow arrows indicate additional spontaneous tumors detected starting from D42.

See also Figures S1 and S2.

(Figure S2A). With a single injection, we were able to perform longitudinal imaging for 4 to 6 weeks, depending on the animal. As we performed imaging analyses for longer time (up to 84 days), a second injection of ExiTron nano 12000 contrast agent was required. After a second injection, in livers we observed a contrast deviation, coherent with an additional accumulation of the contrast agent in Kupffer cells (Figure S2B). Unlike, no significant variations were observed in tumors and the contrast was stable over time (Figure S2C).

The mouse cohorts used in this study and the overall described procedures are illustrated in Figure 1A (see Table S1 for details). A first cohort of six *Alb-R26^Met* mice carrying liver tumors was selected for longitudinal imaging to follow the evolution over time of a total of 15 tumors of different size. PC-CT images acquired
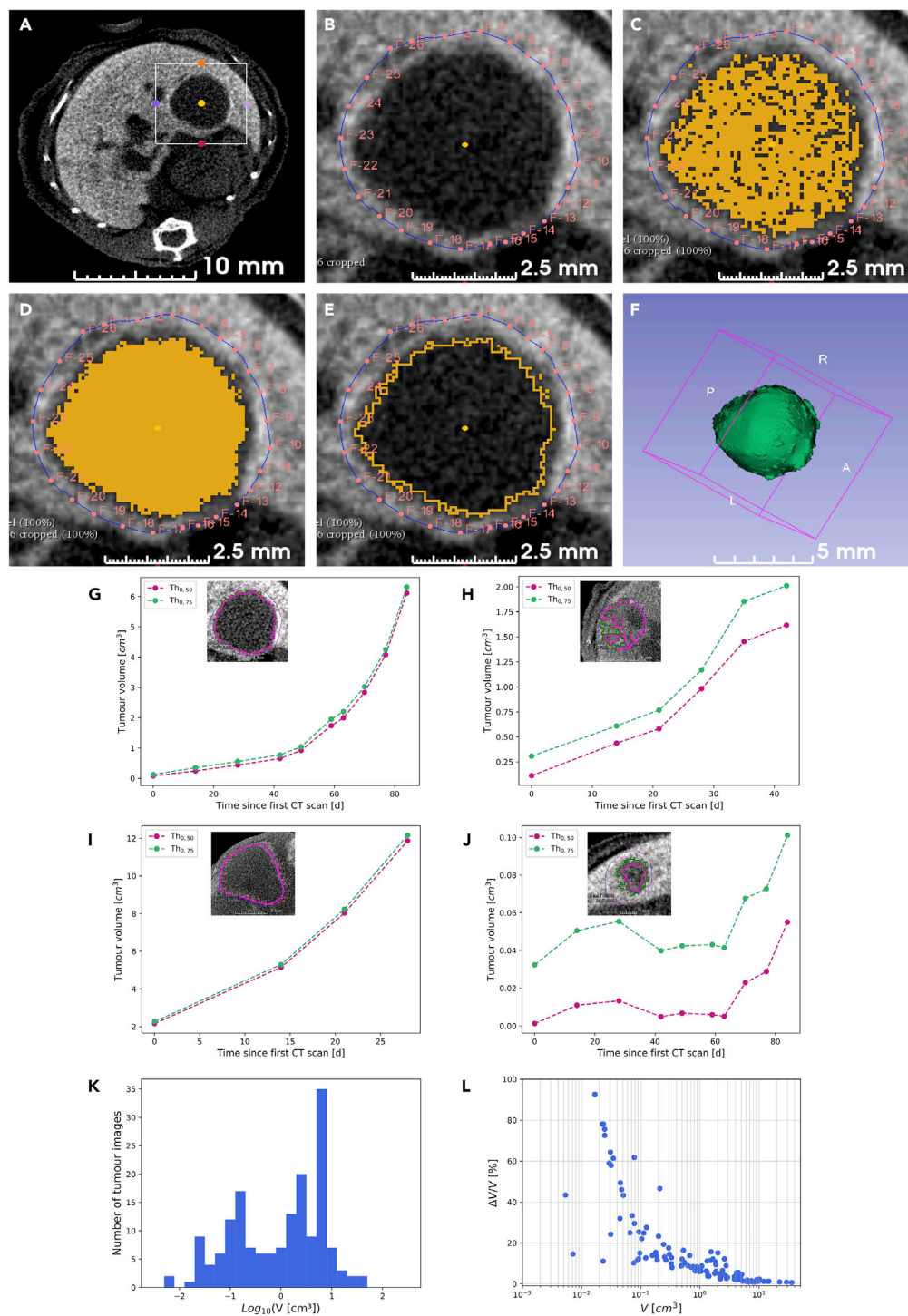
Figure 2. Establishment of a Processing Protocol for Quantitative Measurement of Tumor Volume

(A–F) Images exemplifying the semiautomatic segmentation protocol we followed for tumor volume measurements. The region of interest enclosing the tumor to analyze for quantifications (A) was processed with manual demarcation of the area of segmentation by means of red fiducial markers (B) and application of the predefined contrast threshold to select voxels with a value inferior to the contrast threshold (C). Morphological smoothing to connect the area of voxels was then applied (D), and segmented area was defined according to the predefined contrast threshold (E). Images corresponding to the whole tumor were processed, and values were merged for a 3D reconstruction of the tumor volume (F).

Figure 2. *Continued*

(G–J) Graphs reporting representative examples of longitudinal follow-up of tumor volume growth, corresponding to the largest tumor reported in Figure 1B (G; tumor M1-T4), a medium tumor (H; tumor M5-T1), a big tumor (I; tumor M4-T1), and a small tumor (J; tumor M1-T3). Tumor volume measurements are shown for the two defined contrast thresholds, $Th_{0.50}$ (pink) and $Th_{0.75}$ (green). Images shown in each panel correspond to transverse slices at the tumor maximal diameter acquired at D49 (G and J), D21 (H), and D15 (I); the two-contrast thresholds applied are reported on images.

(K) Histogram of the overall measured tumor volumes, defined as $V = (V_{0.50} + V_{0.75})/2$.

(L) Graph reporting the tumor volume uncertainty, defined as $\Delta V = (V_{0.75} - V_{0.50})/2$. Note that major uncertainties were observed mainly for tumors with a volume less than 10^{-1} cm^3.

See also Figure S3.

with the PIXSCAN-FLI prototype allowed clear detection of neoplastic areas, which appeared without contrast agent with respect to the liver tissue (Figure 1B). Next, we performed a series of processing steps of acquired images for qualitative and quantitative analyses. To quantify the tumor volume, we elaborated a semiautomatic segmentation protocol using the open software 3D Slicer. This segmentation protocol is based on contrast thresholds, in Hounsfield units (HU), defined relative to the liver CT value (HU_L) and the tumor CT value (HU_T): $Th_q = HU_T + q (HU_L - HU_T)$, with $0 < q < 1$. The liver CT value was measured at each scan, being variable with time, whereas the tumor value was constant and assumed equal to 130 HU, which corresponds to the liver CT value without contrast agent, as estimated in a control mouse sample (Figures S2B and S2C). After a manual selection of the region including the tumor (Figures 2A–2F), the volumes $V_{0.50}$ and $V_{0.75}$ below the thresholds at $q = 0.50$ and $q = 0.75$, respectively, were automatically extracted using the segmentation tools provided by 3D Slicer (Figures 2G–2J). These tools permitted to select pixels below a given threshold (Threshold Effect) and to smoothen the segmented volume by discarding isolated pixels and connecting adjacent segmented regions (Remove Island Effect; Figures 2A–2F). The threshold at $q = 0.5$ corresponds to the mid-CT value between healthy high-contrasted liver tissue and tumor tissue, which can be considered as the natural threshold to select between the two densities. However, as the tumor boundaries appeared to be slightly irregular, as illustrated by a partial inclusion of the contrast agent, we have also considered a more inclusive threshold at $q = 0.75$. The volumes $V_{0.75}$ and $V_{0.50}$ differed significantly for small tumors only, which appeared less uniform than bigger tumors, furthermore, with an unfavorable surface to volume ratio (Figure S3). Then, the volume was defined as $V = (V_{0.75} + V_{0.50})/2$ and the volume uncertainty as $\Delta V = (V_{0.75} - V_{0.50})/2$, which actually reflects the tumor contrast inhomogeneity, hence the uncertainty associated to the volume estimation based on the threshold method. We were able to detect tumors starting from about 2.5 mm diameter (corresponding to 0.5×10^{-2} cm^3 of tumor volume; Figure 2K). The volume uncertainty was larger for small tumors (Figure 2L), which were less contrasted (Figure 2J), although it decreased below 20% for volumes higher than 0.1 cm^3.

Long-Term Longitudinal PC-CT Imaging Applied to the *Alb-R26^Met* Genetic Model Revealed Distinct Kinetics in Liver Tumor Growth at Initiation and Evolution Phases

As reported above, the *Alb-R26^Met* HCC model corresponds to the "proliferative-progenitor" HCC patient subgroup (Arechederra et al., 2018; Fan et al., 2017). We revisited a set of data from the *Alb-R26^Met* tumors related to (1) qPCR expression of 96 HCC markers (Fan et al., 2017), (2) phosphokinome analysis of 23 signals (Fan et al., 2017), and (3) methylome of CpG islands (Arechederra et al., 2018). These analyses revealed that even though the *Alb-R26^Met* tumors clearly segregate from control livers, they belong to a broad cluster (Figures 3A–3C). This may reflect the heterogeneity reported among patients with HCC even when belonging to the same subgroup (Cancer Genome Atlas Research Network. Electronic address: wheeler@bcm.edu; Cancer Genome Atlas Research Network, 2017; Llovet et al., 2016; Zucman-Rossi et al., 2015). We therefore reasoned that the *Alb-R26^Met* cancer model could be an appropriate system to evaluate the dynamics of tumors from the initiation stage toward their progression.

We processed imaging data to establish the kinetics of growth of each individual tumor in *Alb-R26^Met* mice (Figure 3D). Concerning tumors above 10^{-1} cm^3, we observed a comparable trend in tumor volume increase over time, corresponding to an exponential growth with a tumor doubling time ranging from 10 to 30 days (Figures 3E–3G). The only exception was M4-T2, a rather big tumor (0.5×10^1 cm^3 at day 0), for which the doubling time was about 60 days. Overall, the median tumor doubling time amounted to 15.9 ± 5.3 days. Concerning small tumors (below 0.5×10^{-1} cm^3 at day 0), their behavior over time was rather heterogeneous. Of five tumors we observed an increase in size in one tumor since its detection (M3-T1), whereas for the other four tumors the size remained unchanged for several weeks (Figures 3D and 4). Intriguingly, whereas M1-T2, M1-T3, and M3-T2 tumors started
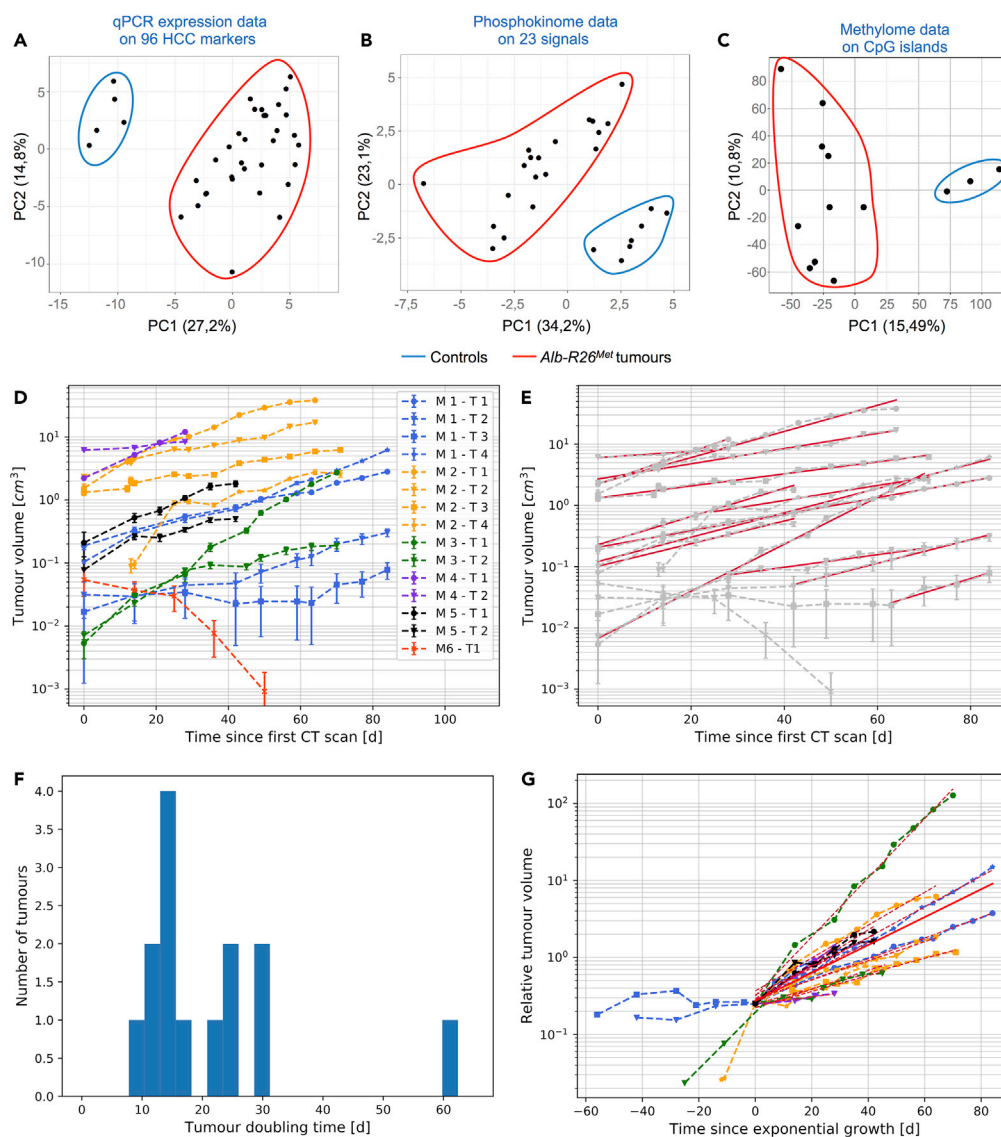
Figure 3. Molecular Heterogeneity and Growth Dynamics of Liver Tumors Modeled in the *Alb-R26^Met* Mice

(A–C) Graphs reporting Principal Component Analysis (PCAs) of control livers and *Alb-R26^Met* tumors using qPCR expression data on 96 HCC markers (A), phosphokinome data on 23 signaling proteins (expression and phosphorylation levels; B), and methylome data on CpG islands (C). Note that tumor samples, distinct from the control samples, form a wider cluster, recapitulating the molecular heterogeneity observed in HCC patient subgroups.

(D) Graph reporting longitudinal quantitative measurements of tumor volumes for the 15 monitored tumors in analyzed mice (see Table S1). Tumor volume was determined according to the semiautomatic protocol illustrated in Figure 2. Tumors with the corresponding mice are indicated on the right. Bars are the maximal volume variation estimated as the half of the difference between volumes calculated for the contrast thresholds $Th_{0.50}$ and $Th_{0.75}$.

(E) Graph reporting the exponential growth modeled by $V(t) = V_0 \exp(\lambda t)$, λ being the tumor growth constant. In (D and E) note the spontaneous partial regression of tumor M6-T1.

(F) Histogram of the tumor doubling time for the 15 tumors analyzed by longitudinal measurement. The tumor doubling time was calculated as $\tau_D = \ln 2/\lambda$. The median of distribution amounts to 15.9 ± 5.3 days.

(G) Graph reporting the relative tumor volume since exponential growth (time zero in the graph).

In (D and E) the data are defined as $V = (V_{0.50} + V_{0.75})/2$ and $\Delta V = (V_{0.75} - V_{0.50})/2$, represented as mean ± SEM.

to grow after about 42, 63, and 28 days, respectively, we observed a spontaneous partial regression of M6-T1 tumor (Figures 4B and 4C). Spontaneous regressions of liver tumors are occasionally observed in patients (Saito et al., 2014).
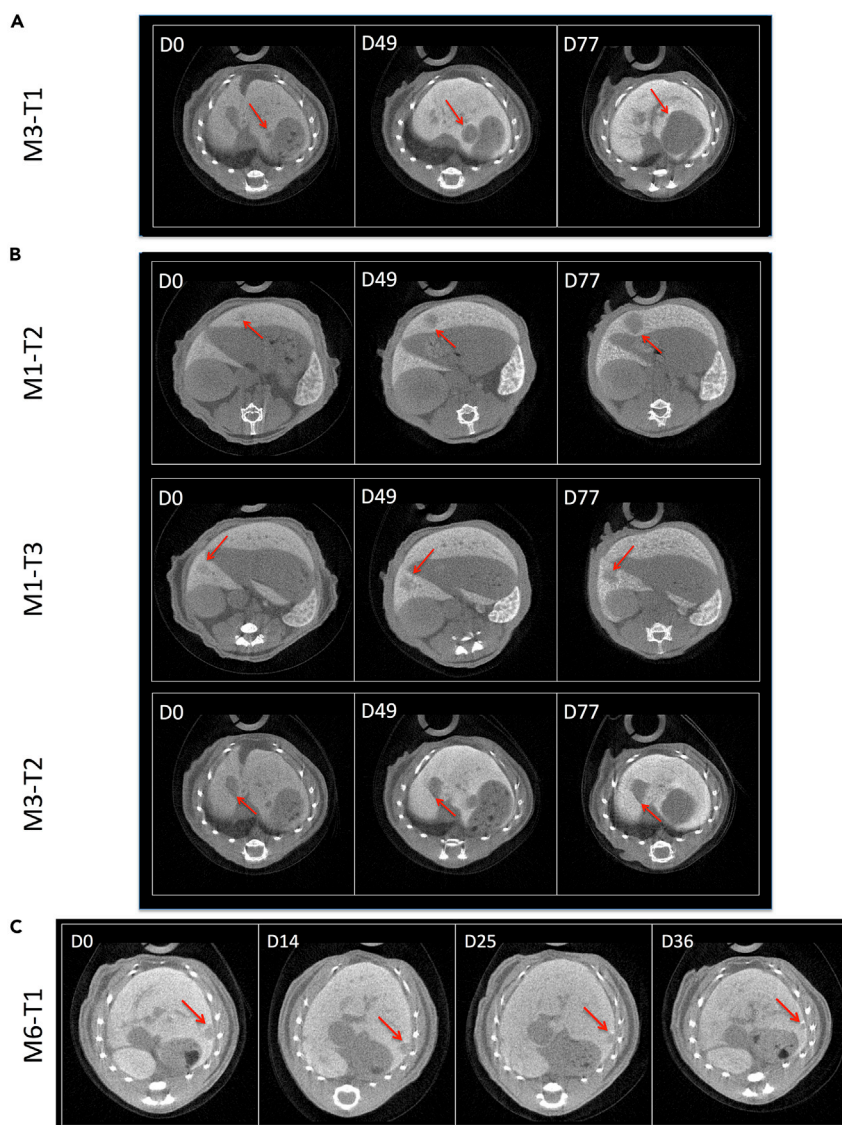
Figure 4. Detection of Liver Tumors Starting from 0.5×10^{-2} cm^3 of Tumor Volume and Assessment of Their Evolution with the PIXSCAN-FLI PC-CT Prototype

(A) Tumor with fast progressive growth in size.

(B) Tumors with very slow progression in size.

(C) Tumor with spontaneous partial regression.

Longitudinal PC-CT Imaging Provided Insight on Anticancer Treatment Effects and the Associated Modifications of the Tumor Environment

Next, we aimed at assessing through longitudinal imaging the dynamics of tumor evolution during anticancer drug treatments. We have previously reported that the *Alb-R26^{Met}* HCC model recapitulates resistance to sorafenib (Fan et al., 2017), a multispecific kinase inhibitor approved as a first-line therapy for HCC (Llovet et al., 2008; Xie et al., 2012). Combining phosphokinome screen outcomes with bioinformatics and with an "educated guess" drug screen, we previously identified new synthetic lethal interactions. One of those involved the combined inhibition of MEK and BCL-XL (Fan et al., 2017). This drug combination treatment is effective on *Alb-R26^{Met}* HCC cells both *in vitro* and in xenografts of nude mice (Fan et al., 2017). Therefore, we first performed PC-CT imaging on a group of mice to identify a cohort of six *Alb-R26^{Met}* mice carrying endogenous liver tumors (for a total of seven tumors), which were then treated with the MEK plus BCL-XL inhibitors. We carried out longitudinal imaging over a period of 40 days during which
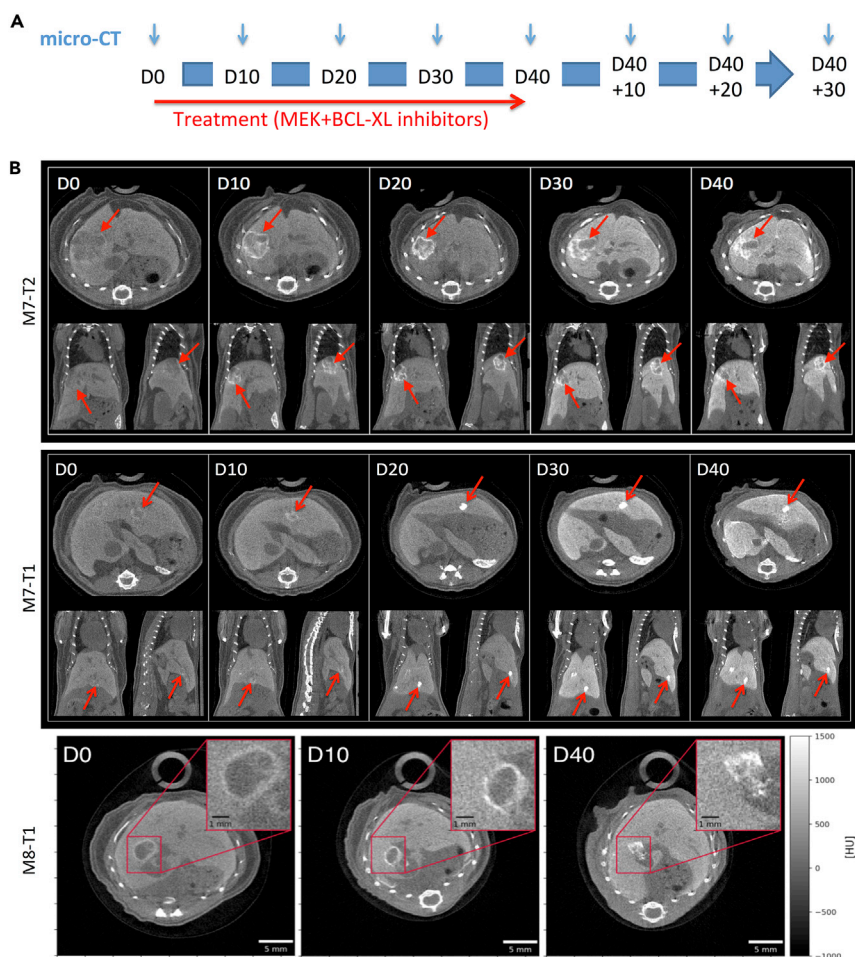
Figure 5. Longitudinal PC-CT *In Vivo* Imaging of Liver Tumor Dynamics in *Alb-R26*[Met] Mice Treated with a Combination of MEK and BCL-XL Inhibitors

(A) Schematic representation of the longitudinal *in vivo* imaging studies that we performed in *Alb-R26*[Met] mice to measure tumor response following MEK and BCL-XL targeting.

(B) Examples of longitudinal monitoring of liver tumor regression in *Alb-R26*[Met] mice treated with MEK and BCL-XL inhibitors. Three tumor examples are reported: tumors M7-T2, M7-T1, and M8-T1. For each day of monitoring, transversal (top), coronal (left bottom), and sagittal (right bottom) slices are shown. The red arrows indicate the tumor during treatment. Once treatment started, note a hyper-contrasted area appearing already at D10 inside and around the tumor, with an enhanced intensity at later time point of treatment. The insets in the lower panels show an enlargement of the tumor, illustrating the highly contrasted area.

mice were treated with this drug combination (Figure 5A). Overall, we gathered a complete set of data corresponding to five tumors in four mice, as two mice died before the treatment was completed, likely due to the overall complexity of the manipulation (Table S1). Qualitative and quantitative analyses revealed a progressive regression of tumor volume in *Alb-R26*[Met]-treated mice (Figures 5B and 6). Remarkably, the tumor volume regressed about 80% as soon as after 10 days of treatment, reaching a regression between 92% and 100% at the end of treatment (Figures 5B and 6). Concerning tumor M10-T1, with a volume of $0.15 \times 10^2 \, \text{cm}^3$ before treatment (day 0), combined MEK and BCL-XL inhibition blocked its progression, with a 35% reduction 10 days after treatment and then stabilized at 15% in subsequent measurements (Figures 6A–6C). Intriguingly, at the first time point of imaging after treatment (D10), we observed a hyper-contrasted zone inside the tumor and in the surrounding region, which became more pronounced at D20 and remained intense until the end of the treatment (Figures 5B and 6; orange volume in 6B and C). The corresponding signal quantification revealed an apparent correlation between the hyper-contrasted volume and the amplitude of tumor regression (Figures 6B and 6C). Collectively, these results showed how PC-CT longitudinal imaging allows quantitative evaluations of drug effects on endogenous tumors. Moreover, our
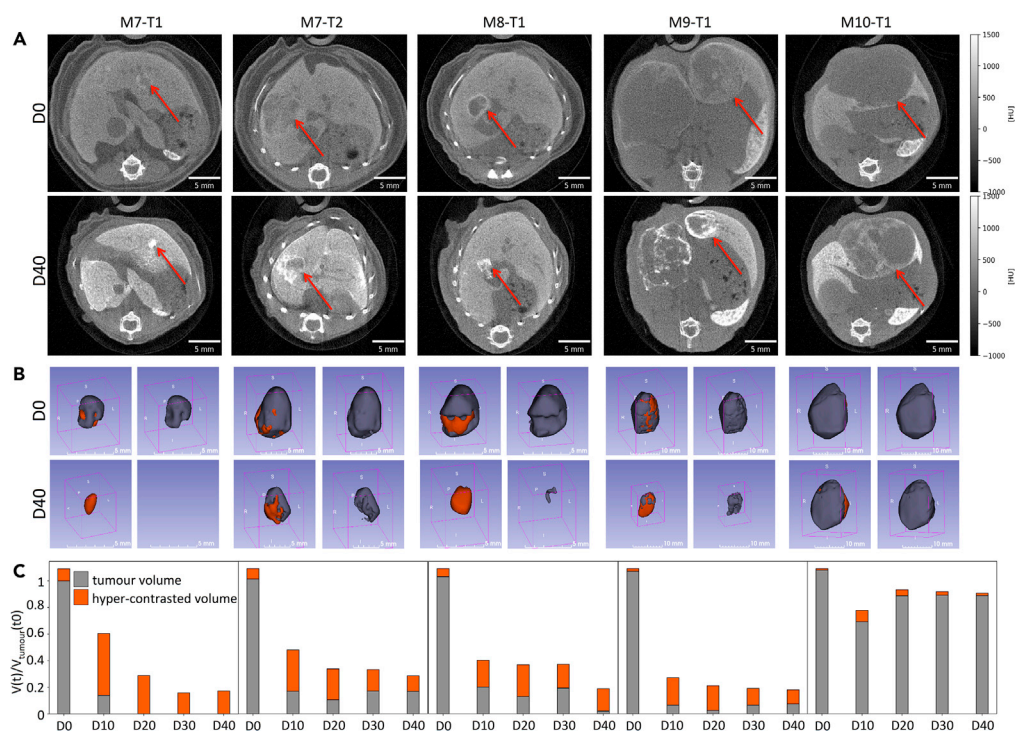
Figure 6. Qualitative and Quantitative PC-CT Measurements of *Alb-R26*^Met^ Liver Tumors in Mice Treated with MEK and BCL-XL Inhibitors

(A) Images corresponding to transverse slices at maximum diameter of five independent tumors before (D0) and at the end of the treatment with MEK + BCL-XL inhibitors (D40).

(B) 3D reconstructions of tumor volumes before (D0) and at the end of the treatment with MEK + BCL-XL inhibitors (D40). On the left, tumor (gray) and high-contrasted (orange) volumes are reported. On the right, images correspond to tumor volumes (gray).

(C) Graphs reporting longitudinal imaging measurements of tumor (gray) and high-contrasted (orange) volumes before (D0) and during drug treatments. Note the dramatic reduction of tumor volumes after treatment in four tumors (M7-T1, M7-T2, M8-T, M9-T1). For a big tumor (M10-T1), treatment stopped its growth, with only a slight regression during treatment. In this tumor, a very small high-contrasted area was observed.

findings revealed that MEK + BCL-XL inhibition is effective not only on HCC xenografts in nude mice (Fan et al., 2017) but also on endogenous tumors in *Alb-R26*^Met^ mice.

Next, we extended PC-CT longitudinal imaging studies with the PIXSCAN-FLI prototype to evaluate the dynamics of tumors in *Alb-R26*^Met^ mice once treatment was stopped (Figure 5A). Concerning M7-T1 tumor, we found a complete regression and no relapse was observed even 30 days after discontinuation of treatment (Figures 7 and 8). Concerning the other four tumors, in which regression was not complete after treatment, we observed a progressive increase in tumor volume over time after cessation of treatment, although with different kinetics (Figures 7 and 8). M8-T1 and M9-T1 tumors did not reach the volume observed before beginning of the treatment. In contrast, 30 days after discontinuation of the treatment, the M7-T2 tumors has returned to their original value (measured before treatment), and M10-T1, the less responding tumor, rapidly increased in volume (Figure 8). Concerning the hyper-contrasted region inside the tumor and in the surrounding area, we recorded a progressive decrease of its volume when tumor started to relapse (Figure 8; orange volume in 8B and C). Together, these longitudinal *in vivo* imaging analyses performed over a 70-day period spanning an initial treatment phase followed by a resting phase, exemplify the relevance of evaluating treatment effectiveness in preclinical assays with a powerful imaging system like the PIXSCAN-FLI PC-CT prototype. Of note, this equipment offers the possibility of performing multiple measurements over time due to the limited X-ray dose used for the imaging session.

As reported above, our imaging studies highlighted that regression of tumors during drug treatment was accompanied by the appearance of highly contrasted zones within the tumor and in the surrounding
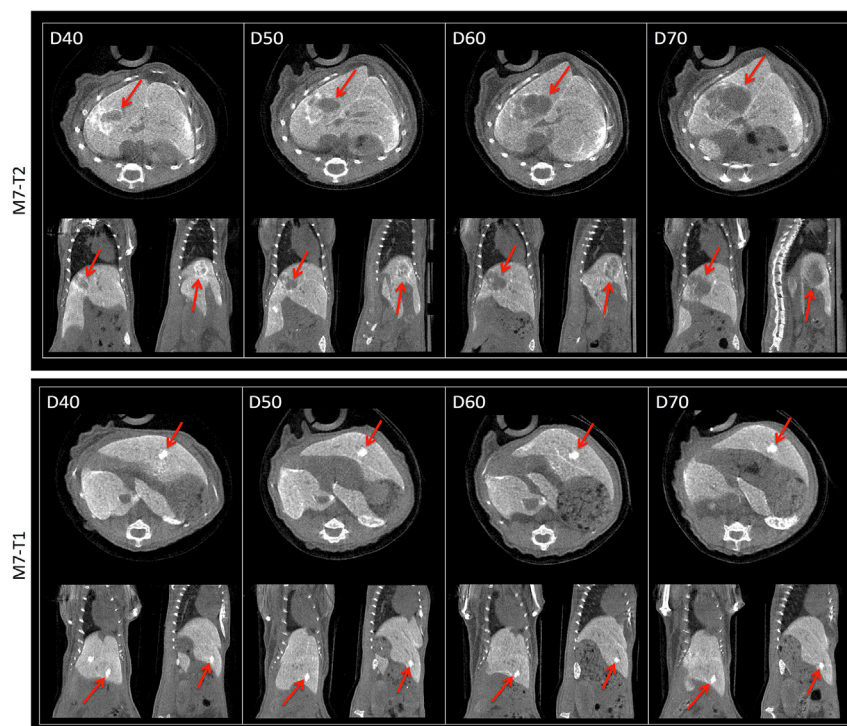
Figure 7. Longitudinal PC-CT *In Vivo* Imaging of Liver Tumor Dynamics in *Alb-R26^Met* Mice Once Treatment with Targeted Drug Combination Was Discontinued

Examples of longitudinal monitoring of liver tumor growth in *Alb-R26^Met* mice from the last day of treatment (D40) over time (D50, D60, D70). M7-T2 tumor started to grow (top), whereas M7-T1 tumor growth was not observed and a high-contrasted area persisted over time. For each day of monitoring, transversal (top), coronal (left bottom), and sagittal (right bottom) slices are shown. The red arrows indicate the corresponding tumor. Note that these two tumors recorded in the same mouse were both sensitive to the treatment, although the M7-T2 relapsed, whereas the M7-T1 did not.

region. As ExiTron nano 12000 is phagocytized and accumulated by macrophages, we hypothesized that these highly contrasted zones could correspond to accumulation of macrophages in the environment of these regressing tumors. We explored this possibility by performing histological studies of *Alb-R26^Met* tumors during the drug-driven regression phase. In particular, a third cohort of tumor-bearing *Alb-R26^Met* mice were treated for 15 days with MEK plus BCL-XL inhibitors, imaging was performed before (D0) and at the end of the treatment (D15), then mice where sacrificed for histological analyses. H&E staining of *Alb-R26^Met* liver tumor sections confirmed the presence of HCC and revealed an enrichment of macrophage hyperplasia in the microenvironment of regressing tumors in contrast to tumors from untreated mice (Figures 9A–9H). Immunohistological analyses using anti-F4/80 antibodies, which recognize macrophages, evidenced the presence of highly enlarged macrophages surrounding the regressing tumors in *Alb-R26^Met*-treated mice in contrast to tumors from untreated animals (Figures 9I–9L). Anti-cleaved Caspase-3 immunostaining revealed the presence of dying cells in tumors from *Alb-R26^Met*-treated mice in contrast to untreated animals (Figures 9M–9P). Thus, highly contrasted regions in the microenvironment of regressing tumors, revealed by PC-CT imaging, correspond to an enrichment of highly enlarged macrophages.

DISCUSSION

Hybrid pixel technology was originally invented for charged particle tracking in high-energy physics experiments. At the end of the nineties, this technology started to be applied also to X-ray imaging both for material science and biomedical imaging (Delpierre, 2014; Wermes, 2005). In this study, we exploited for the first time the hybrid pixel camera XPAD3 for *in vivo* imaging in a biomedical context. The PC-CT PIXSCAN-FLI prototype, equipped with a XPAD3 camera, permitted to provide optimized imaging acquisition parameters (50 kV/500 µA, 0.6 mm Al filtering, 720 projections) and to reach a good compromise between tumor detectability and the radiation dose. Indeed, the achieved dose of 180 mGy per
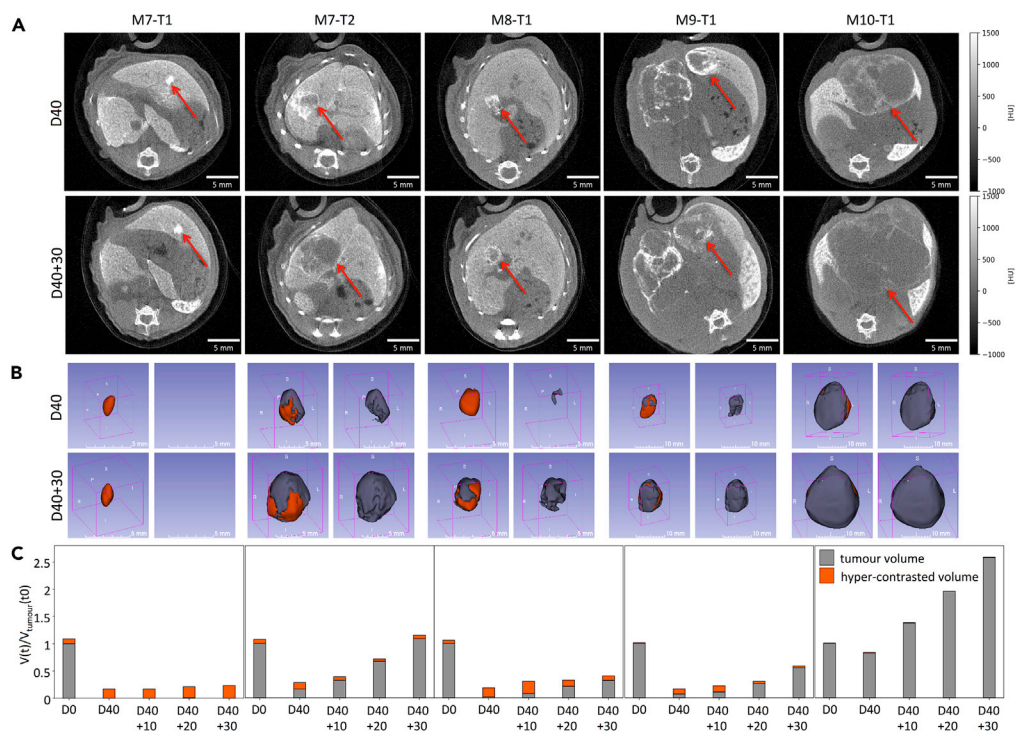
Figure 8. Qualitative and Quantitative PC-CT Measurements of *Alb-R26^Met* Liver Tumors in Mice after Treatment with Targeted Drug Combinations

(A) Images corresponding to transverse slices at tumor maximum diameter of five independent tumors at the end of treatment (D40) and 30 days later (D40 + 30).

(B) 3D reconstructions of tumor volumes at D40 (end of treatment) and after 30 days (D40 + 30). On the left, tumor (gray) and high-contrasted (orange) volumes are reported. On the right, images correspond to tumor volumes (gray).

(C) Graphs reporting longitudinal imaging measurements of tumor (gray) and high-contrasted (orange) volumes at D0 (before treatment), at the end of treatment (D40), and during the following 30 days. Complete regression was observed for M7-T1 tumor, whereas regrowth occurred for the other four tumors, although with a variable speed and kinetics. Images of tumors at D40, already shown in Figure 5A, are also shown here for direct comparison with tumor images at D40 + 30.

scan allowed performing longitudinal studies over several months without observing any major consequences in mice. Moreover, the short acquisition time (7.5 min/mouse) was compatible with a simultaneous follow-up of a relatively large mouse cohort. For future developments, the use of CdTe hybrid pixels instead of Si hybrid pixels (Buton et al., 2014) would allow to reach similar imaging results with a reduced dose of about 60 mGy, benefitting of a much higher X-ray detection efficiency of the CdTe sensors (Cassol et al., 2015). Concerning detectability of small objects such as tumors in animal models, a critical factor is the intrinsic contrast and the image noise. Image noise could be reduced at the photon statistics level by the PC property of the XPAD3 camera, whereas optimal intrinsic contrast was achieved using targeted contrast agents such as the ExiTron nano 12000. We chose this agent for several properties previously reported, including (1) the *in vivo* stability over time, (2) the superior performance compared with other contrast agents, (3) the small volume of injection required, and (4) the lack of hepatotoxicity and of pro-inflammatory cytokine release (Boll et al., 2011, 2013; Liu et al., 2019; Mannheim et al., 2016; Wathen et al., 2013). In our studies, we showed that the ExiTron nano 12000 not only induced a significant increase in X-ray attenuation in the liver (about a factor of 5) but also permitted to reveal unexpected changes in the environment of treatment tumors. Thus, the combination of PC-CT with suitable contrast agents can provide both anatomical and functional information, which deserves further exploitation for medical and pre-clinical imaging. Future longitudinal PC-CT analyses of liver tumors, like those in the *Alb-R26^Met* mouse model, using other contrast agents, such as non-toxic nanodroplets loaded with iodine with high-contrast properties specific for hepatocytes and with strong liver persistence (Anton et al., 2017), will widen this approach for quantitative follow-up of tumor evolution and regression while testing anticancer treatments. Furthermore, in a perspective of clinical application, this imaging approach could be particularly relevant
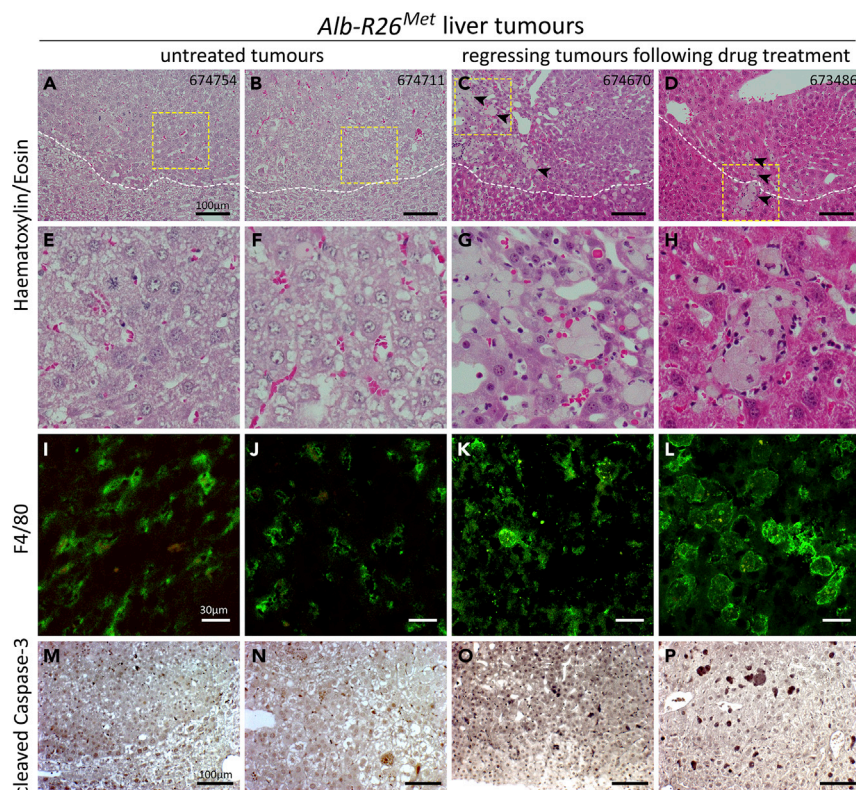
Figure 9. Enlarged Macrophages Accumulate in the Microenvironment of *Alb-R26^Met* Regressing Tumors during MEK plus BCL-XL Inhibition

(A–H) H&E staining of tumor sections from *Alb-R26^Met* mice either untreated (A, B, E, and F) or treated with MEK and BCL-XL inhibitors (C, D, G, and H). In (C and D) note extensive peritumoral macrophage hyperplasia (arrowheads) surrounding locally invasive well-differentiated HCC cells. The dotted lines depict the border between the tumor and the normal parenchyma. (E–H) High magnifications of the area indicated by the yellow squares in (A–D).

(I–L) Immunohistological staining showing anti-F4/80-positive macrophages in the peritumoral area of tumors. Note highly enlarged macrophages in the microenvironment of drug-driven regressing tumors (K and L) compared with tumors from untreated *Alb-R26^Met* mice (I and J).

(M–P) Immunohistological staining with anti-cleaved Caspase-3 in the peritumoral area of untreated (M and N) and treated (O and P) *Alb-R26^Met* mice.

The mice IDs are indicated on the top right corners of (A–D). Scale bars are indicated.

for the early diagnosis and monitoring of liver tumors in human patients, according to guidelines of the American Association for the Study of Liver Diseases and the European Association for the Study of the Liver.

The application of longitudinal PC-CT imaging with the PIXSCAN-FLI prototype on the *Alb-R26^Met* cancer model with spontaneous liver tumor formation allowed us to explore the dynamics of tumors at distinct steps of the oncogenic program: the initiation, the evolution, the response to treatments, and the later follow-up. The high performance and quality of our PC-CT detection was particularly appropriate to determine the behavior of tumors at the very first initiation phase (with a size of about 0.5×10^{-2} cm^3) when they spontaneously originate in the liver. We found that whereas one tumor rapidly evolved by increasing its size, with a growth rate comparable to those of larger tumors, three others remained in an apparent latent phase, as illustrated by an unchanged size for 1–2 months. It is tempting to speculate that such heterogeneity in the behavior of small tumors might reflect the severity of alterations at the root of the tumorigenic events. Indeed, different combinatorial alterations lead to distinct "fitness": strong alterations can lead to a rapid tumor growth, whereas weak alterations may result in a latency state whose evolution is conditioned by the acquisition of additional modifications. Differences in "fitness" on tumorigenic events have been recently exemplified by a forward genetic screening in mice, exploring genetic specificity in cooperation for tumorigenesis (Rogers et al., 2018; Wangensteen et al., 2018). Another example comes from a

transposon mutagenesis screen we performed in the *Alb-R26^{Met}* genetic model, which uncovered distinct modes of cooperation with RTKs (Fan et al., 2019). Nevertheless, alterations of distinct genes appeared to not have equivalent strengths in tumorigenesis acquisition, as illustrated by the variety of tumor size formed following targeting distinct tumor suppressors. Future studies using a large cohort of mice would permit extending these findings and corroborate them with statistical analysis to determine whether the behaviors of small tumors are equally distributed between long-term latency versus rapid growth and to clarify the frequency of spontaneous tumor regression we observed. It would be particularly interesting as well to combine imaging data with screen outcomes of distinct tumors to uncover how tumor latency/ growth matches with (epi)genetic/transcriptome/proteome signatures.

Concerning the evolution of growing tumors modeled by the *Alb-R26^{Met}* mice, we recorded an overall trend of tumor doubling time ranging between 10 and 30 days, with a median of 15.9 $\pm$ 5.3 days. Indeed, we observed that the doubling time for each tumor remained constant over time. It is tempting to speculate that the sets of alterations ensuring tumor growth at early phases might determine the speed of tumor growth over time. Concerning our longitudinal studies performed by treating mice with a drug combination targeting MEK and BCL-XL, a synthetic lethal interaction in HCC cells we previously reported *in vitro* and in nude mice xenografts (Fan et al., 2017), our studies showed its remarkable effects also on *Alb-R26^{Met}* endogenous tumors. The only exception was for the rather big tumor, for which MEK + BCL-XL inhibition did not lead to significant regression, although it clearly blocked its growth. These results support the relevance to further explore the MEK + BCL-XL drug combination through preclinical studies in a translational perspective for human HCC patient subsets. In addition, beside complete regression for a relatively small tumor, our results showed that once the treatment was stopped, the other three medium-sized tumors regrew after an approximately 90% reduction of their volume. Future studies combining imaging data with phosphoproteomic profiles of distinct tumors would be instrumental to clarify whether and to what extent tumors maintain sensitivity to MEK + BCL-XL treatment over time. These approaches may also reveal resistance mechanisms, which can be targeted by subsequent treatments.

Our longitudinal imaging in mice treated with MEK and BCL-XL inhibitors also uncovered a remarkable remodeling of the tumor microenvironment, as illustrated by the accumulation of macrophages in regressing tumors. Such accumulation of macrophages is coherent with a process of removing dying cancer cells caused by drug treatment. Nevertheless, it is well known that macrophages can contribute to tumor destruction or facilitate tumor growth and metastasis, depending on their phenotype (Ostrand-Rosenberg, 2008). Macrophages are a primary source of several mediators such as cytokines, chemokines, and growth factors (Chawla et al., 2011; Stienstra et al., 2010). These factors can influence the cross talk between cancer and immune cells, the presence of cytotoxic T-cells targeting the tumor and/or of tumor-promoting immune cells fostering cancer cell proliferation and invasion (Becht et al., 2016), as well as angiogenesis (Ehling et al., 2014). As our studies were performed in tumor-bearing immunocompetent mice, future studies will determine whether tumor regression targeting MEK and BCL-XL can be further potentiated by an immunotherapy to achieve maximal anticancer response. Immunotherapy is gaining tremendous attention for its potential as anticancer treatment. Current cancer immunotherapies focus on overcoming ineffective immune reactivity against solid tumors, either by global activation of the immune system or by manipulation of immune-regulatory molecules in the tumor microenvironment, including the so-called immune checkpoints. The latter aims at increasing the ratio of cytotoxic T cells over suppressive cells. Several new treatment possibilities are currently under investigation to exploit better the immunotherapy potential in clinics.

Among these, the programmed death-1 (PD-1) system received tremendous attention and several preclinical/ clinical studies support the potential of its modulation for therapy, including for HCC treatment (Foerster et al., 2018; Greten and Sangro, 2017; Inarrairaegui et al., 2018; Ruiz de Galarreta et al., 2019; Tacke, 2017; Wu et al., 2009). As a subset of patients with HCC still showed relapse after anti-PD-1 treatment (Ruiz de Galarreta et al., 2019), combining toxic drugs to target cancer cells and checkpoint blockade might maximize the therapeutic responses (Champiat et al., 2014; Harding, 2018). It would be relevant to assess whether the detrimental effects of MEK plus BCL-XL targeting on HCC cells accompanied by an increased tumor clearance by macrophages could be potentiated upon immune checkpoint modulation. Whether these tumor-loaded macrophages conjointly acquire increased immunogenic properties will require further investigations.

Future effective targeted molecular therapies will likely emerge using agents combined to target simultaneously cancer and immune cells (Champiat et al., 2014). Nevertheless, this requires implementing

knowledge on (1) remodeling processes of immune cell types occurring when cancer cells are targeted by drugs, (2) optimal timing of simultaneous drug administration, and (3) beneficial constant versus pulses of treatments over time to eradicate cancer, or transform it into a chronic disease. The PIXSCAN-FLI proto-type for longitudinal PC-CT imaging of spontaneous liver tumors like those modeled by the clinically relevant *Alb-R26^Met* mice represents a valuable system to explore these aspects and to design new therapeutic interventions combining cancer cell targeting agents with immunotherapy for achieving maximal anti-cancer responses.

Limitations of the Study

As the *Alb-R26^Met* model recapitulates the molecular characteristics of the "proliferative-progenitor" HCC patient subgroup as well as the molecular heterogeneity that characterizes these patients, we would predict that knowledge acquired through these studies is relevant to the human HCC pathology. However, it would be necessary to corroborate findings by analyzing a large cohort of mice (for example, composed of about 50 animals) for longitudinal measurement of several parameters at distinct phases of the oncogenic program. Moreover, the combination of imaging data with screen outcomes for individual tumors will be essential to elucidate how tumor dynamics matches with molecular signatures.

METHODS

All methods can be found in the accompanying Transparent Methods supplemental file.

SUPPLEMENTAL INFORMATION

Supplemental Information can be found online at https://doi.org/10.1016/j.isci.2019.10.015.

ACKNOWLEDGMENTS

AUTHOR CONTRIBUTIONS

F.C. conceived this interdisciplinary study; designed, supervised, and performed imaging analysis; performed data analysis and interpretation; and contributed to write the manuscript. L.P. performed imaging, data analysis, and interpretation and provided input on studies and on the manuscript. S.R. contributed to imaging studies and histological analysis. M.D. contributed to imaging acquisition and reconstruction. Y.B. contributed to imaging reconstruction. M.A. performed computational work with *Alb-R26^Met* screen outcomes, data analysis, and interpretation and provided inputs on studies and on the manuscript. N.A-A. supervised histological studies and contributed to data interpretation. L.C. performed histological studies, data analysis, and interpretation. C.L. contributed to interpret histological analysis and staining and provided inputs on pathological studies. S.F. performed imaging studies, data analysis, and interpretation. L.B. performed imaging studies, data analysis, and interpretation. F.L. contributed to experimental work for histological studies and interpretation and provided inputs on studies. R.D. contributed to establishing the *Alb-R26^Met* mouse model and provided inputs on studies. B.G. contributed to supervise imaging studies. T.L. provided inputs on studies. C.M. designed and supervised imaging studies, analyzed and interpreted data; ensured financial support; and contributed to write the manuscript. F.M. conceived this interdisciplinary study; designed and supervised the biological studies, contributed to experimental work, analyzed and interpreted data; ensured financial support; and wrote the manuscript.

DECLARATION OF INTERESTS

The authors declare no competing interest.

REFERENCES

Anton, N., Parlog, A., Bou About, G., Attia, M.F., Wattenhofer-Donze, M., Jacobs, H., Goncalves, I., Robinet, E., Sorg, T., and Vandamme, T.F. (2017). Non-invasive quantitative imaging of hepatocellular carcinoma growth in mice by micro-CT using liver-targeted iodinated nano-emulsions. Sci. Rep. 7, 13935.

Arechederra, M., Daian, F., Yim, A., Bazai, S.K., Richelme, S., Dono, R., Saurin, A.J., Habermann, B.H., and Maina, F. (2018). Hypermethylation of gene body CpG islands predicts high dosage of functional oncogenes in liver cancer. Nat. Commun. 9, 3164.

Ashton, J.R., West, J.L., and Badea, C.T. (2015). In vivo small animal micro-CT using nanoparticle contrast agents. Front. Pharmacol. 6, 256.

Ballabriga, R., Alozy, J., Campbell, M., Frojdh, E., Heijne, E.H.M., Koenig, T., Llopart, X., Marchal, J., Pennicard, D., Poikela, T., et al. (2016). Review of hybrid pixel detector readout ASICs for spectroscopic X-ray imaging. J. Instrum. 11, 1–31.

Becht, E., Giraldo, N.A., Dieu-Nosjean, M.C., Sautes-Fridman, C., and Fridman, W.H. (2016). Cancer immune contexture and immunotherapy. Curr. Opin. Immunol. 39, 7–13.

Boll, H., Nittka, S., Doyon, F., Neumaier, M., Marx, A., Kramer, M., Groden, C., and Brockmann, M.A. (2011). Micro-CT based experimental liver imaging using a nanoparticulate contrast agent: a longitudinal study in mice. PLoS One 6, e25692.

Boll, H., Figueiredo, G., Fiebig, T., Nittka, S., Doyon, F., Kerl, H.U., Nolte, I., Forster, A., Kramer, M., and Brockmann, M.A. (2013). Comparison of Fenestra LC, ExiTron nano 6000, and ExiTron nano 12000 for micro-CT imaging of liver and spleen in mice. Acad. Radiol. 20, 1137–1143.

Bour, G., Martel, F., Goffin, L., Bayle, B., Gangloff, J., Aprahamian, M., Marescaux, J., and Egly, J.M. (2014). Design and development of a robotized system coupled to microCT imaging for intratumoral drug evaluation in a HCC mouse model. PLoS One 9, e106675.

Buton, C., Dawiec, A., Graber-Bolis, J., Arnaud, K., Bérar, J.-F., Blanc, N., Boudet, N., Clémens, J.-C., Debarbieux, F., Delpierre, P., et al. (2014). Comparison of three types of XPAD3.2/CdTe single chip hybrids for hard X-ray applications in material science and biomedical imaging. Nucl. Instr. Methods Phys. Res. A 758, 44–56.

Cancer Genome Atlas Research Network. Electronic address: wheeler@bcm.edu; Cancer Genome Atlas Research Network (2017). Comprehensive and integrative genomic characterization of hepatocellular carcinoma. Cell 169, 1327–1341.e23.

Cassol, F., Clemens, J.C., Hemmer, C., and Morel, C. (2009). Imaging performance of the hybrid pixel detectors XPAD3-S. Phys. Med. Biol. 54, 1773–1789.

Cassol, F., Portal, L., Graber-Bolis, J., Perez-Ponce, H., Dupont, M., Kronland-Martinet, C., Boursier, Y., Blanc, N., Bompard, F., Boudet, N., et al. (2015). K-edge imaging with the XPAD3 hybrid pixel detector, direct comparison of CdTe and Si sensors. Phys. Med. Biol. 60, 5497–5511.

Cassol, F., Dupont, M., Kronland-Martinet, C., Ouamara, H., Dawiec, H., Boursier, Y., Bonissent, A., Clémens, J.-C., Portal, L., Debarbieux, F., et al. (2016). Characterization of the imaging performance of a micro-CT system based on the photon counting XPAD3/Si hybrid pixel detectors. Biomed. Phys. Eng. Express 2, 025003.

Champiat, S., Ileana, E., Giaccone, G., Besse, B., Mountzios, G., Eggermont, A., and Soria, J.C. (2014). Incorporating immune-checkpoint inhibitors into systemic therapy of NSCLC. J. Thorac. Oncol. 9, 144–153.

Chawla, A., Nguyen, K.D., and Goh, Y.P.S. (2011). Macrophage-mediated inflammation in metabolic disease. Nat. Rev. Immunol. 11, 738–749.

Das, N.M., Hatsell, S., Nannuru, K., Huang, L., Wen, X., Wang, L., Wang, L.H., Idone, V., Meganck, J.A., Murphy, A., et al. (2016). In vivo quantitative microcomputed tomographic analysis of vasculature and organs in a normal and diseased mouse model. PLoS One 11, e0150085.

Delpierre, P. (2014). A history of hybrid pixel detectors, from high energy physics to medical imaging. J. Instrum. 9, 1–12.

Ehling, J., Bartneck, M., Wei, X., Gremse, F., Fech, V., Mockel, D., Baeck, C., Hittatiya, K., Eulberg, D., Luedde, T., et al. (2014). CCL2-dependent infiltrating macrophages promote angiogenesis in progressive liver fibrosis. Gut 63, 1960–1971.

Fan, Y., Richelme, S., Avazeri, E., Audebert, S., Helmbacher, F., Dono, R., and Maina, F. (2015). Tissue-specific gain of RTK signalling uncovers selective cell vulnerability during embryogenesis. PLoS Genet. 11, e1005533.

Fan, Y.N., Arechederra, M., Richelme, S., Daian, F., Novello, C., Calderaro, J., Di Tommaso, L., Morcrette, G., Rebouissou, S., Donadon, M., et al. (2017). A phosphokinome-based screen uncovers new drug synergies for cancer driven by liver-specific gain of nononcogenic receptor tyrosine kinases. Hepatology 66, 1644–1661.

Fan, Y.N., Bazai, S.K., Daian, F., Arechederra, M., Richelme, S., Temiz, N.A., Yim, A., Habermann, B.H., Dono, R., Largaespada, D.A., et al. (2019). Evaluating the landscape of gene cooperativity with receptor tyrosine kinases in liver tumorigenesis using transposon-mediated mutagenesis. J. Hepatol. 70, 470–482.

Foerster, F., Hess, M., Gerhold-Ay, A., Marquardt, J.U., Becker, D., Galle, P.R., Schuppan, D., Binder, H., and Bockamp, E. (2018). The immune

contexture of hepatocellular carcinoma predicts clinical outcome. Sci. Rep. 8, 5351.

Genestine, M., Caricati, E., Fico, A., Richelme, S., Hassani, H., Sunyach, C., Lamballe, F., Panzica, G.C., Pettmann, B., Helmbacher, F., et al. (2011). Enhanced neuronal Met signalling levels in ALS mice delay disease onset. Cell Death Dis. 2, e130.

Greten, T.F., and Sangro, B. (2017). Targets for immunotherapy of liver cancer. J. Hepatol. https://doi.org/10.1016/j.jhep.2017.09.007.

Hanson, K.M. (1979). Detectability in computed tomographic images. Med. Phys. 6, 441–451.

Harding, J.J. (2018). Immune checkpoint blockade in advanced hepatocellular carcinoma: an update and critical review of ongoing clinical trials. Future Oncol. 14, 2293–2302.

Inarrairaegui, M., Melero, I., and Sangro, B. (2018). Immunotherapy of hepatocellular carcinoma: facts and hopes. Clin. Cancer Res. 24, 1518–1524.

Krenkel, O., and Tacke, F. (2017). Liver macrophages in tissue homeostasis and disease. Nat. Rev. Immunol. 17, 306–321.

Liu, C.N., Morin, J., Dokmanovich, M., Bluette, C.T., Goldstein, R., Manickam, B., and Bagi, C.M. (2019). Nanoparticle contrast-enhanced micro-CT: a preclinical tool for the 3D imaging of liver and spleen in longitudinal mouse studies. J. Pharmacol. Toxicol. Methods 96, 67–77.

Llovet, J.M., Ricci, S., Mazzaferro, V., Hilgard, P., Gane, E., Blanc, J.F., de Oliveira, A.C., Santoro, A., Raoul, J.L., Forner, A., et al. (2008). Sorafenib in advanced hepatocellular carcinoma. N. Engl. J. Med. 359, 378–390.

Llovet, J.M., Zucman-Rossi, J., Pikarsky, E., Sangro, B., Schwartz, M., Sherman, M., and Gores, G. (2016). Hepatocellular carcinoma. Nat. Rev. Dis. Primers 2, 16018.

Mannheim, J.G., Schlichthaerle, T., Kuebler, L., Quintanilla-Martinez, L., Kohlhofer, U., Kneilling, M., and Pichler, B.J. (2016). Comparison of small animal CT contrast agents. Contrast Media Mol. Imaging 11, 272–284.

Martiniova, L., Schimel, D., Lai, E.W., Limpuangthip, A., Kvetnansky, R., and Pacak, K. (2010). In vivo micro-CT imaging of liver lesions in small animal models. Methods 50, 20–25.

Ostrand-Rosenberg, S. (2008). Immune surveillance: a balance between protumor and antitumor immunity. Curr. Opin. Genet. Dev. 18, 11–18.

Pandit, P., Johnston, S.M., Qi, Y., Story, J., Nelson, R., and Johnson, G.A. (2013). The utility of micro-CT and MRI in the assessment of longitudinal growth of liver metastases in a

preclinical model of colon carcinoma. Acad. Radiol. 20, 430–439.

Pangaud, P., Basolo, S., Boudet, N., Berar, J.F., Chantepie, B., Delpierre, P., Dinkespiler, B., Hustache, S., Menouni, M., and Morel, C. (2007). XPAD3: a new photon counting chip for X-ray CT-scanner. Nucl. Instrum. Meth. A 571, 321–324.

Rogers, Z.N., McFarland, C.D., Winters, I.P., Seoane, J.A., Brady, J.J., Yoon, S., Curtis, C., Petrov, D.A., and Winslow, M.M. (2018). Mapping the in vivo fitness landscape of lung adenocarcinoma tumor suppression in mice. Nat. Genet. 50, 483–486.

Rothe, J.H., Rudolph, I., Rohwer, N., Kupitz, D., Gregor-Mamoudou, B., Derlin, T., Furth, C., Amthauer, H., Brenner, W., Buchert, R., et al. (2015). Time course of contrast enhancement by micro-CT with dedicated contrast agents in normal mice and mice with hepatocellular carcinoma: comparison of one iodinated and two nanoparticle-based agents. Acad. Radiol. 22, 169–178.

Ruiz de Galarreta, M., Bresnahan, E., Molina-Sanchez, P., Lindblad, K.E., Maier, B., Sia, D., Puigvehi, M., Miguela, V., Casanova-Acebes, M., Dhainaut, M., et al. (2019). beta-catenin activation promotes immune escape and resistance to anti-PD-1 therapy in hepatocellular carcinoma. Cancer Discov. 9, 1124–1141.

Saito, T., Naito, M., Matsumura, Y., Kita, H., Kanno, T., Nakada, Y., Hamano, M., Chiba, M., Maeda, K., Michida, T., et al. (2014). Spontaneous regression of a large hepatocellular carcinoma with multiple lung metastases. Gut Liver 8, 569–574.

Schambach, S.J., Bag, S., Schilling, L., Groden, C., and Brockmann, M.A. (2010). Application of micro-CT in small animal imaging. Methods 50, 2–13.

Stienstra, R., Saudale, F., Duval, C., Keshtkar, S., Groener, J.E., van Rooijen, N., Staels, B., Kersten, S., and Muller, M. (2010). Kupffer cells promote hepatic steatosis via interleukin-1beta-dependent suppression of peroxisome proliferator-activated receptor alpha activity. Hepatology 51, 511–522.

Tacke, F. (2017). Targeting hepatic macrophages to treat liver diseases. J. Hepatol. 66, 1300–1312.

Taguchi, K., and Iwanczyk, J.S. (2013). Vision 20/20: single photon counting x-ray detectors in medical imaging. Med. Phys. 40, 100901.

Tonges, L., Ostendorf, T., Lamballe, F., Genestine, M., Dono, R., Koch, J.C., Bahr, M., Maina, F., and Lingor, P. (2011). Hepatocyte growth factor protects retinal ganglion cells by increasing neuronal survival and axonal regeneration in vitro and in vivo. J. Neurochem. 117, 892–903.

Wangensteen, K.J., Wang, Y.J., Dou, Z., Wang, A.W., Mosleh-Shirazi, E., Horlbeck, M.A., Gilbert, L.A., Weissman, J.S., Berger, S.L., and Kaestner, K.H. (2018). Combinatorial genetics in liver repopulation and carcinogenesis with a in vivo CRISPR activation platform. Hepatology 68, 663–676.

Wathen, C.A., Foje, N., van Avermaete, T., Miramontes, B., Chapaman, S.E., Sasser, T.A., Kannan, R., Gerstler, S., and Leevy, W.M. (2013). In vivo X-ray computed tomographic imaging of

soft tissue with native, intravenous, or oral contrast. Sensors (Basel) 13, 6957–6980.

Wermes, N. (2005). Pixel detectors for tracking and their spin-off in imaging applications. Nucl. Instrum. Meth. A. 541, 150–165.

Will, O.M., Damm, T., Campbell, G.M., von Schonfells, W., Acil, Y., Will, M., Chalaris-Rissmann, A., Ayna, M., Drucker, C., and Gluer, C.C. (2017). Longitudinal micro-computed tomography monitoring of progressive liver regeneration in a mouse model of partial hepatectomy. Lab. Anim. 51, 422–426.

Willekens, I., Lahoutte, T., Buls, N., Vanhove, C., Deklerck, R., Bossuyt, A., and de Mey, J. (2009). Time-course of contrast enhancement in spleen and liver with Exia 160, Fenestra LC, and VC. Mol. Imaging Biol. 11, 128–135.

Wu, K., Kryczek, I., Chen, L.P., Zou, W.P., and Welling, T.H. (2009). Kupffer cell suppression of CD8(+) T cells in human hepatocellular carcinoma is mediated by B7-H1/programmed death-1 interactions. Cancer Res. 69, 8067–8075.

Xie, B., Wang, D.H., and Spechler, S.J. (2012). Sorafenib for treatment of hepatocellular carcinoma: a systematic review. Dig. Dis. Sci. 57, 1122–1129.

Zucman-Rossi, J., Villanueva, A., Nault, J.C., and Llovet, J.M. (2015). Genetic landscape and biomarkers of hepatocellular carcinoma. Gastroenterology 149, 1226–1239.e4.

Supplemental Information

Tracking Dynamics of Spontaneous

Tumors in Mice Using Photon-Counting

Computed Tomography

Franca Cassol, Loriane Portal, Sylvie Richelme, Mathieu Dupont, Yannick Boursier, Maria Arechederra, Nathalie Auphan-Anezin, Lionel Chasson, Caroline Laprie, Samantha Fernandez, Laure Balasse, Fabienne Lamballe, Rosanna Dono, Benjamin Guillet, Toby Lawrence, Christian Morel, and Flavio Maina

SUPPLEMENTAL MATERIALS
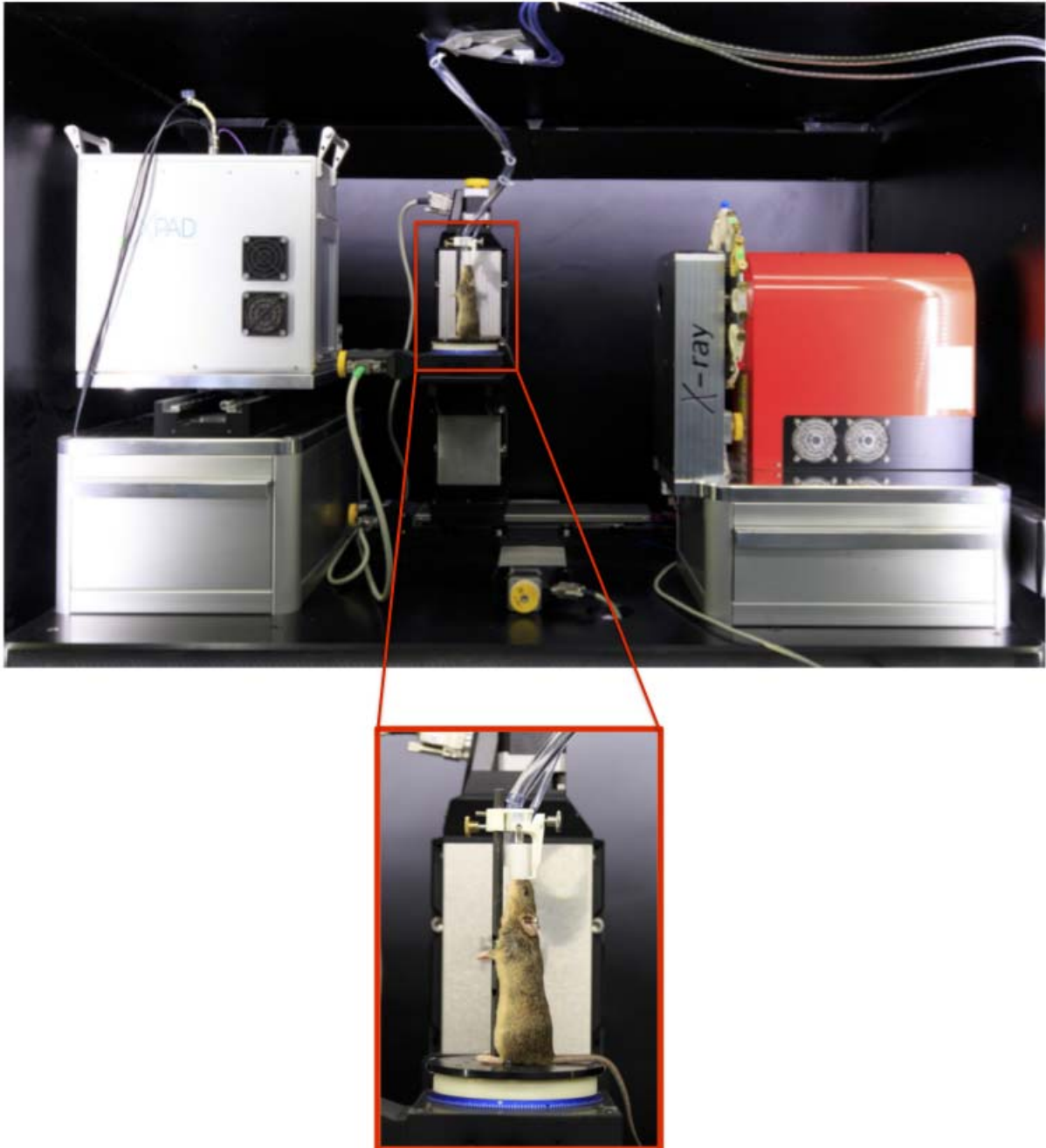

Figure S1. Photography of the PIXSCAN-FLI PC-CT prototype equipped with a XPAD3/Si hybrid pixel camera (top) showing the position of mice during recoding (bottom), Related to Figure 1.
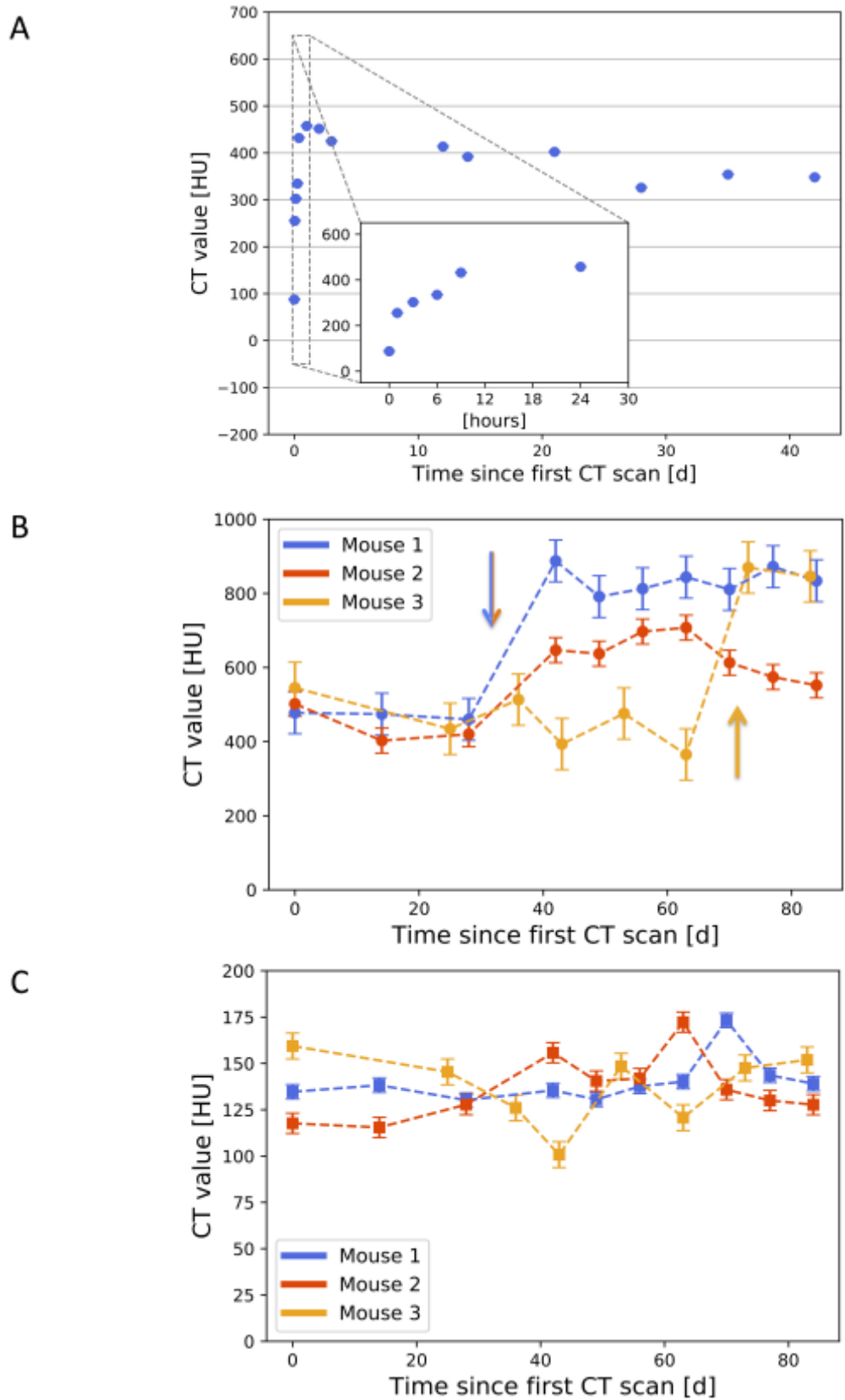
Figure S2. Graphs reporting CT values in livers and tumors, Related to Figure 1. (A) Graph reporting the fast increase of the liver CT value (in Hounsfield units) after injection of 4 μL/g mouse of

ExiTron^{TM} nano 12000. (B, C) Graphs reporting longitudinal monitoring of the CT value (in Hounsfield units) in the liver (B) and in the tumor region (C) for three representative mice. We observed a contrast deviation in livers after a second injection of the ExiTron^{TM} nano 12000 (indicated by arrows), coherent with an additional accumulation of the contrast agent in Kupffer cells. Instead, the tumor contrast was stable overtime, and no significant variations were observed.

Figure S3. Panels correspond to transverse slices at the tumor maximal diameter, Related to Figure 2. Images were acquired at D49 (A and D), D21 (B), and D15 (C), and are also reported in

Figure 2G-J. Images are reported without (left) and with the two-contrast thresholds applied (right). Tumor volume measurements are shown for the 2 defined contrast thresholds: $Th_{0.50}$ (pink) and $Th_{0.75}$ (green).
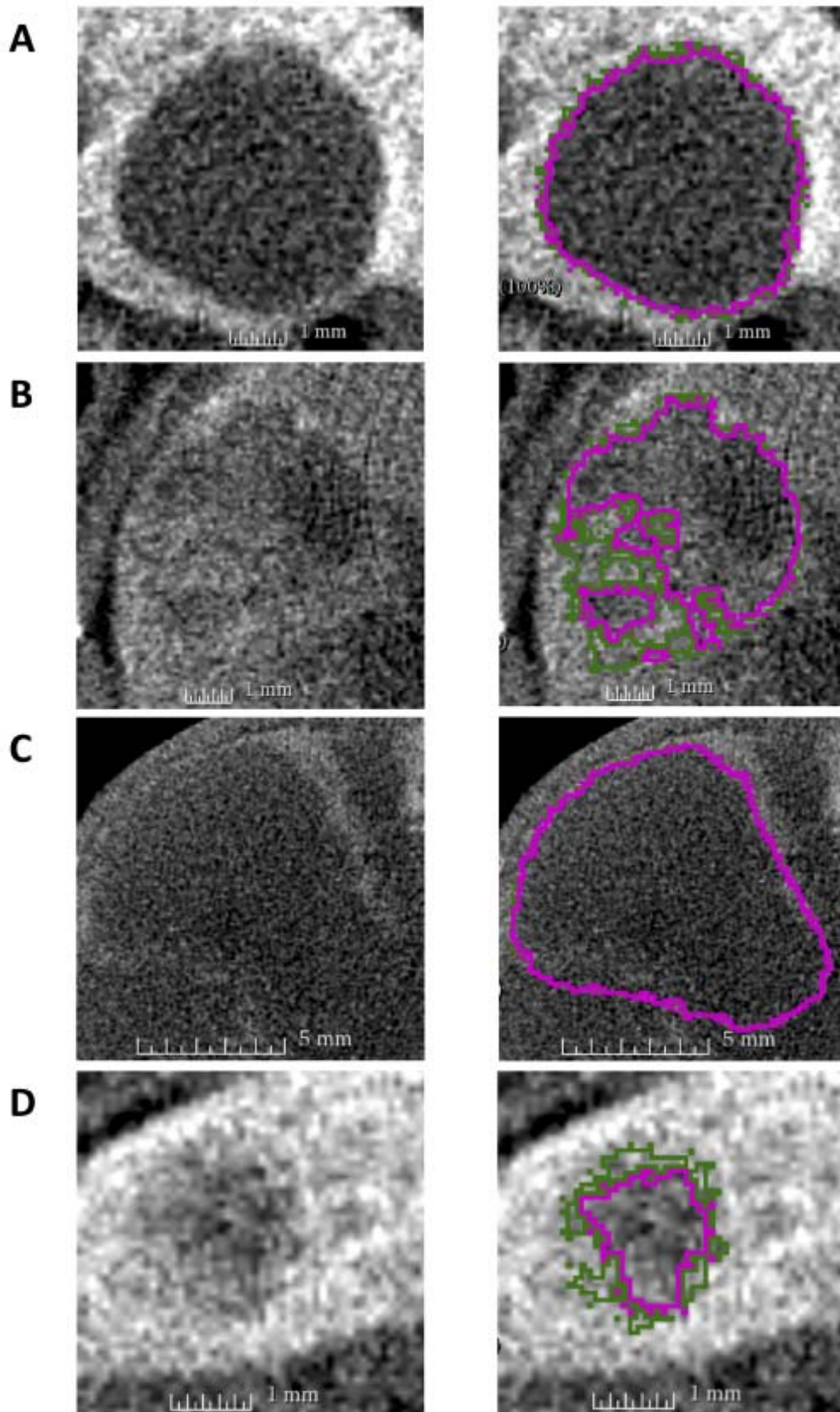
cohorts	tumor	mouse	ID	follow-up time (days)	% of tumor regression after treatment
1° cohort	M1-T1	M1	672 472	84	
	M1-T2				
	M1-T3				
	M1-T4				
	M2-T1	M2	672 399	77	
	M2-T2				
	M2-T3				
	M2-T4				
	M3-T1	M3	670 320	77	
	M3-T2				
	M4-T1	M4	672 524	28	
	M4-T2				
	M5-T1	M5	672 526	42	
	M5-T2				
	M6-T1	M6	672 403	71	
2° cohort	M7-T1	M7	672 517	70	100%
	M7-T2				92%
	M8-T1	M8	673 823	70	99%
	M9-T1	M9	673 822	70	96%
	M10-T1	M10	672 398	70	21%
	M11-T1	M11	672 536	28 (D)	75% (at 20 days)
	M12-T1	M12	673 830	34 (D)	23% (at 30 days)
3° cohort		M13	674 670	15	
		M14	673 598	15	
		M15	673 486	15	

Table S1. Table summarizing the tumors and the corresponding mice used for longitudinal PC-CT imaging, Related to Figure 1. Mice found dead (FD) during the manipulation are indicated. The percentage of tumor regression in the cohort of treated mice is reported. For mice found dead (M11 and M12), the percentage of tumor regression correspond to the last imaging analysis performed.

mouse	genotype	untreated/treated	case	sample	histological description	diagnosis
674638	*Alb-R26^Met*	untreated	19-0171	liver	Normal lobular architectecture	
674642	*Alb-R26^Met*	untreated	19-0172	liver	Normal lobular architectecture	
674712	*Alb-R26^Met*	untreated	19-0174	liver	Normal lobular architectecture	
674711	*Alb-R26^Met*	untreated	19-0173	tumor T1	Focal ill-defined nodular hepatocytic proliferative foci with loss of lobular architecture and locally infiltrative growth (carcinoma)	Hepatocytic carcinoma, well differentiated
674749	*Alb-R26^Met*	untreated	19-0176	tumor T2	Focal well-defined, expansile, nodular hepatocytic proliferative foci with loss of lobular architecture	Hepatocytic adenoma
674754	*Alb-R26^Met*	untreated	19-0177	tumor T1	Focal well-defined, expansile, nodular hepatocytic proliferative foci with loss of lobular architecture	Hepatocytic adenoma
			19-0178	tumor T1C	Focal ill-defined nodular hepatocytic proliferative foci with loss of lobular architecture and locally infiltrative growth (carcinoma)	Hepatocytic carcinoma, well differentiated
			19-0179	tumor T3	Focal well-defined, expansile, nodular hepatocytic proliferative foci with loss of lobular architecture	Hepatocytic adenoma
674763	*Alb-R26^Met*	untreated	19-0181	tumor T1	Focal well-defined, expansile, nodular hepatocytic proliferative foci with loss of lobular architecture	Hepatocytic adenoma
			19-0182	tumor T2	Focal well-defined, expansile, nodular hepatocytic proliferative foci with loss of lobular architecture	Hepatocytic adenoma
673486	*Alb-R26^Met*	treated with MEK+BCL-XL inhibitors	18-0668	tumor T1A	Focal nodular hepatocytic proliferative foci with loss of lobular architecture (adenoma). Multifocal Kupffer cell hyperplasia	Hepatocytic adenoma, multifocal necrosis

			18-0671	tumor T3B	Localized proliferation of hepatocytes, phenotypically similar to adjacent hepatocytes without persistent lobular architecture (no visible portal tracts) : adenoma Kupffer cell hypertrophy	Hepatocytic adenoma
			18-0672	liver	Normal. Mild vacuolar centrolobular degeneration Kupffer cells hypertrophy	
673598	*Alb-R26^Met*	treated with MEK+BCL-XL inhibitors	18-0670	liver C	Normal lobular architecture Focal marked Kupffer cell hypertrophy and hyperplasia with enlarged cells	Focal marked Kupffer cells hyperplasia (with abundant intracellular material)
			18-0669	tumor T1A	Medio and centrobular hypertrophy with karyomegaly, mild Kupffer cell hypertrophy	
674670	*Alb-R26^Met*	treated with MEK+BCL-XL inhibitors	18-0665	liver C	Normal lobular architectecture	
			18-0666	tumor T1C	Well delineated hepatic nodule, locally infiltrating the adjacent parenchyma Loss of normal lobular architecture Well differentiated hepatocytes, forming trabeculae Focal necrotic foci (1x0.5 mm) Peritumoral Kupffer cells hyperplasia	Hepatocarcinoma, well differentiated, locally necrotic Peritumoral kupffer cell hyperplasia

Table S2. Table summarizing the mice used for histological studies, Related to Figure 9.

TRANSPARENT METHODS

Ethics Statement. All procedures with animals were performed in accordance with the European Community Council Directive of 22 September 2010 on the protection of animals used for experimental purposes (2010/63/EU). The experimental protocols were carried out in compliance with institutional Ethical Committee guidelines for animal research (comité d'éthique pour l'expérimentation animale – Comité d'éthique de Marseille) and in compliance with French law, under an agreement number E1305521, Ministère de l'enseignement supérieur de la recherche et de l'innovation. Mice were kept in a dedicated pathogen free facility, with a light/dark cycle, and in cages with an enrichment environment. Mice received Safe Complete Care Competence (SAFE A04) as complete aliment *ad libitum*. The project authorization of Maina laboratory is: APAFIS #8214-2016121417291352.v5 delivered by the "Ministère de l'Enseignement Supérieur, de la Recherche et de l'Innovation".

Alb-R26^Met **mice.** The generation of the *R26^stopMet* mice (international nomenclature *Gt(ROSA)26Sor^tm1(Actb-Met)Fmai*) carrying a conditional mouse-human chimeric *Met* transgene into the *Rosa26* locus, and the genotyping procedures were previously reported (Fan et al., 2015; Genestine et al., 2011; Tonges et al., 2011). The mouse line expressing Cre recombinase under the *Alb* promoter (*B6.Cg-Tg(Alb-cre)21Mgn/J*) was obtained from the Jackson Laboratory. *Alb-R26^Met* mice were generated by crossing the *R26^stopMet* and *Alb-R26^Met* mice (Arechederra et al., 2018; Fan et al., 2017; Fan et al., 2019). Mice were maintained in a 50% mixed background of 129/SV and C57BL6, and genotyped by PCR analysis of genomic DNA as previously reported (Fan et al., 2015; Genestine et al., 2011). Only males were used for these studies. From a total of 41 mice aged between 58 and 68 weeks at the first PC-CT imaging analysis, 15 mice with one or multiple liver tumors were used for these studies (Table S1). This number of mice was chosen to support our studies with several tumors from independent animals while respecting ethical recommendations to limit the number of mice for experimental manipulations.

PIXSCAN-FLI PC-CT prototype. The PC-CT PIXSCAN-FLI prototype (Figure S1) is contained in a lead/steel box of dimensions 139.5 cm × 101 cm × 99.5 cm (L × W × H). It is composed of a tungsten

anode X-ray tube Microfocus L12161-07 (Hamamatsu Photonics K.K., Japan) with a 7-50 µm emission spot and a hybrid pixel camera XPAD3 with pixels of 130 µm × 130 µm (Cassol et al., 2009; Pangaud et al., 2007). In front of the X-ray tube, a wheel holding filters of different materials (Al, Cu, Ag, Mo and others) and thicknesses permits further modulation of the cone beam of X-rays. The X-ray camera XPAD3 is composed of eight contiguous horizontal modules slightly tilted vertically and overlapped to avoid dead areas. Each module has a size of 7.5 cm × 1.6 cm and consists of a 500 µm thick Si sensor with 67,200 (560 × 120) pixels of 130 µm × 130 µm bump-bonded to seven chips XPAD3, each of which reading out a matrix of 9,600 (80 × 120) pixels. Thus, the camera has a sensitive surface of 7.5 cm × 11.5 cm and a total of 537,600 pixel. For in vivo imaging, the mouse was placed vertically between the X-ray source and the XPAD3 camera on a rotating platform positioned on a (x,y,z) translation table, as shown in Figure S1. For this study, the platform rotation axis distance from the camera was set to 39 cm, which corresponds to an imaging magnification factor of 1.54 due to the conical geometry of the beam. Tomographic scans were acquired under continuous rotation and continuous irradiation of X-rays generated with 50 kV and 500 µA (50 µm spot size) through 0.6 mm Al filtering, for which the camera detection efficiency amounts approximately to 35%. Mice were analyzed under general anesthesia (Isoflurane [~1.5 vol%]/O_2), which was controlled by a gas anesthesia unit (manufactured by Minerve; France). The dose rate at the mouse position was measured with a dosimeter Diados W 45-150 kV (PTW-Freiburg, Germany). The dose per scan delivered to the mouse was estimated by multiplying the dose rate by the scan duration.

Data processing. Tomographic scans of 720 projections with a 0.5° step, thus covering a full rotation, have been acquired. Spurious measurements (photon counts per pixel) due to dead or miscalibrated pixels, usually less than 2% of the total number of pixels, were detected using the prior acquisition and the processing of 25 dark fields and 25 flat fields. Missing data are recovered by linear interpolation based on the three closest neighbors given by a Voronoï tessellation calculated from the position in three dimensions of the pixels, which encompasses the specific internal tiled geometry of the XPAD3 camera and the global geometric configuration of the PIXSCAN-FLI prototype.

In particular, the geometry of the imaging setup was estimated beforehand through a dedicated minimization procedure based on the scan of rotating steel balls (Khoury et al., 2009). Each projection

was normalized by the mean of the 25 flat fields. The negative logarithm of the results constituting the tomographic scans were first reconstructed with a standard FDK (Feldkamp et al., 1984) algorithm implemented with the standard Ram-Lak filter convolved without apodization in the spatial domain in the open source reconstruction toolkit OpenRTK (Rit et al., 2014) (https://www.openrtk.org/), which delivered volumes of size 588 x 882 x 588 with cubic pixels of size 0.084 mm defined by the cone beam magnification (1.54) of the 0.130 mm detector pixels. The reconstructed image spatial resolution of the system, which was estimated with a QRM-microCT-wire phantom (QRM, Germany), corresponds to a Point Spread Function (PSF) of about 0.125 mm FWHM. The voxel CT values (CTV) are expressed in Hounsfield units (HU) defined as HU = $1000*(CTV - CTV_{water})/CTV_{water}$, where CTV_{water} is the CT value of a volume of water acquired under the same irradiation conditions. The reconstructed volumes were then analyzed with the 3D-Slicer software (https://www.slicer.org) to obtain a quantitative values of the tumor volume. This was achieved with a semiautomatic approach: a manual preliminary volume selection was followed by a reproducible volume quantification based on predefined contrast thresholds.

Principal Component Analysis (PCA) o screen data. For Principal Component Analysis (PCA), we revisited these *Alb-R26^{Met}* screen data: a) qPCR expression of 96 HCC markers (Fan et al., 2017), b) phosphokinome analysis of 23 signals (Fan et al., 2017), and c) methylome of CpG islands (Arechederra et al., 2018). PCA was performed using the Clustvis web tool: https://biit.cs.ut.ee/clustvis/.

In vivo drug administration in *Alb-R26^{Met}* mice. *Alb-R26^{Met}* mice carrying liver tumors were treated daily with intraperitoneal injections of drug combinations (ABT-737: 30 mg/kg; Selumetinib: 30 mg/kg). Concerning the 2° cohort, mice were treated for 40 days and imaging was performed every 10 days up to D70. Concerning the 3° cohort, mice were treated for 15 days, imaging was performed before starting the treatment and at D15. Livers and tumors were dissected and processed for histological analysis.

Histology and immunofluorescence microscopy. For histological analyses, tissues were fixed with 10% buffered formalin (VWR chemical, #9713.5000) for 24h, dehydrated and embedded in paraffin (Fischer histoplast, #6.774060), sectioned, stained with hematoxylin (Fischer, #6765004), and counterstained with eosin (Fischer, #10483750) using an automated Leica autostainer XL. The slides mounted with Entellan (Merck, #1.07961) were examined using a Nikon Eclipse. For immunofluorescent analysis, tissues were embedded in optimum cutting temperature medium (OCT) freezing media (Tissue-Tek, #4583). Consecutive liver sections were blocked for 1 hour in 2% BSA before overnight incubation with primary antibodies: anti-F4/80 (Bio-Rad, #MCA497-647; 1/200). Stained liver sections mounted in ProLong Gold antifade reagent with DAPI (Life Technologies, #P36931) were then analyzed by confocal microscopy using a Zeiss LSM 780. For cleaved Caspase-3 detection, sections were processed as previously reported (Furlan et al., 2012). Briefly, paraffin-embedded sections were deparaffinized, incubated for 20 minutes in epitope unmasking solution (Vector Laboratories), then permeabilized with PBS +0.5% Triton X-100 for 15 min. Endogenous peroxidase was quenched with 3% H_2O_2 in PBS +0.1% Triton X-100 for 15 min. Unspecific binding was then blocked with 10% BSA and 2% donkey serum for 1h at RT. Anti-cleaved Caspase-3 antibodies (Cell Signaling #9661, 1/250) were then applied overnight at 4°C. Endogenous biotin receptors present in livers were blocked by using the avidin-biotin blocking kit (Vector Laboratories). Secondary antibodies (biotinylated-donkey-anti-rabbit; 1/500) were then applied for 1h at RT. Signal amplification was performed using the VECTASTAIN®ABC-kit (Vector Labs).

SUPPLEMENTAL REFERENCES

Feldkamp, L.A., Davis, L.C., and Kress, J.W. (1984). Practical Cone-Beam Algorithm. J Opt Soc Am A *1*, 612-619.

Furlan, A., Lamballe, F., Stagni, V., Hussain, A., Richelme, S., Prodosmo, A., Moumen, A., Brun, C., Del Barco Barrantes, I., Arthur, J.S.*, et al.* (2012). Met acts through Abl to regulate p53 transcriptional outcomes and cell survival in the developing liver. J Hepatol *57*, 1292-1298.

Khoury, R., Bonissent, A., Clements, J.C., Meessen, C., Vigeolas, E., Billault, M., and Morel, C. (2009). A geometrical calibration method for the PIXSCAN micro-CT scanner. J Instrum *4*, P07016.

Rit, S., Oliva, M.V., Brousmiche, S., Labarbe, R., Sarrut, D., and Sharp, G.C. (2014). The Reconstruction Toolkit (RTK), an open-source cone-beam CT reconstruction toolkit based on the Insight Toolkit (ITK). J Phys Conf Ser *489*, 012079.